

Study of CME Propagation in the Inner Heliosphere: SOHO LASCO, SMEI and STEREO HI Observations of the January 2007 Events

D.F. Webb · T.A. Howard · C.D. Fry · T.A. Kuchar · D. Odstrcil · B.V. Jackson ·
M.M. Bisi · R.A. Harrison · J.S. Morrill · R.A. Howard · J.C. Johnston

Received: 5 December 2008 / Accepted: 31 March 2009 / Published online: 17 April 2009
© Springer Science+Business Media B.V. 2009

Abstract We are investigating the geometric and kinematic characteristics of interplanetary coronal mass ejections (ICMEs) using data obtained by the LASCO coronagraphs, the So-

STEREO Science Results at Solar Minimum

Guest Editors: Eric R. Christian, Michael L. Kaiser, Therese A. Kucera, O.C. St. Cyr

Electronic supplementary material The online version of this article (<http://dx.doi.org/10.1007/s11207-009-9351-8>) contains supplementary material, which is available to authorized users.

D.F. Webb (✉) · T.A. Kuchar
Institute for Scientific Research, Boston College, Chestnut Hill, MA, USA
e-mail: david.webb@hanscom.af.mil

D.F. Webb · T.A. Kuchar · J.C. Johnston
Air Force Research Laboratory, Space Vehicles Directorate, Hanscom AFB, MA, USA

T.A. Howard
Air Force Research Laboratory, National Solar Observatory, Sunspot, NM, USA

C.D. Fry
Exploration Physics International, Inc., Huntsville, AL, USA

D. Odstrcil
Cooperative Institute for Research in Environmental Sciences, University of Colorado, Boulder, CO, USA

D. Odstrcil
Space Weather Prediction Center, National Oceanic and Atmospheric Administration, Boulder, CO, USA

B.V. Jackson · M.M. Bisi
Center for Astrophysics and Space Science, University of California-San Diego, La Jolla, CA, USA

R.A. Harrison
Space Physics Division, Space Science and Technology Dept., Rutherford Appleton Laboratory, Chilton, Didcot, Oxfordshire, UK

J.S. Morrill · R.A. Howard
Space Science Division, Code 7663, Naval Research Laboratory, Washington, DC, USA

lar Mass Ejection Imager (SMEI), and the SECCHI imaging experiments on the STEREO spacecraft. The early evolution of CMEs can be tracked by the LASCO C2 and C3 and SECCHI COR1 and COR2 coronagraphs, and the HI and SMEI instruments can track their ICME counterparts through the inner heliosphere. The HI fields of view ($4-90^\circ$) overlap with the SMEI field of view ($> 20^\circ$ to all sky) and, thus, both instrument sets can observe the same ICME. In this paper we present results for ICMEs observed on 24–29 January 2007, when the STEREO spacecraft were still near Earth so that both the SMEI and STEREO views of large ICMEs in the inner heliosphere coincided. These results include measurements of the structural and kinematic evolution of two ICMEs and comparisons with drive/drag kinematic, 3D tomographic reconstruction, the HAFv2 kinematic, and the ENLIL MHD models. We find it encouraging that the four model runs generally were in agreement on both the kinematic evolution and appearance of the events. Because it is essential to understand the effects of projection across large distances, that are not generally crucial for events observed closer to the Sun, we discuss our analysis procedure in some detail.

Keywords Coronal mass ejections · Corona · Interplanetary plasma

1. Introduction

Coronal mass ejections (CMEs) are eruptions of large amounts of mass and embedded magnetic fields from the Sun. CMEs are a major way that the Sun removes magnetic flux and helicity; they may contain over 10^{16} g of plasma and may span tens of degrees of heliospheric latitude and longitude. When CMEs impact Earth they can cause significant geomagnetic activity, such as geomagnetic storms.

Imaging observations of CMEs typically use coronagraphs, which block the direct photospheric light from the Sun leaving the relatively faint surrounding corona. The most successful coronagraph for CME detection is the *Solar and Heliospheric Observatory* (SOHO) Large Angle Spectroscopic Coronagraph (LASCO) (Brueckner *et al.*, 1995) which has detected well over 10^4 CMEs with many of their parameters measured and cataloged (St. Cyr *et al.*, 2000; Yashiro *et al.*, 2004). The interplanetary counterparts of CMEs, or ICMEs (Zhao, 1992; Dryer, 1994) have in the past been studied primarily using *in-situ* observations from various spacecraft (for a recent review see Harrison *et al.*, 2009). However, our emphasis here is on imaging ICME observations which, in the past, have been remotely sensed using interplanetary scintillation techniques (*e.g.*, Hewish, Scott, and Wills, 1964; Ananthakrishnan *et al.*, 1999; Jones *et al.*, 2007), and coarse imaging with the *Helios* white light photometer data (Richter, Leinert, and Planck, 1982; Webb and Jackson, 1990). However, both of these methods used data of very low temporal and spatial resolution. Recently, white light images of ICMEs at much higher resolution have become available. Currently operating are the Solar Mass Ejection Imager (SMEI) (Eyles *et al.*, 2003; Jackson *et al.*, 2004) aboard the *Coriolis* satellite and the Heliospheric Imagers (Harrison *et al.*, 2008; Howard *et al.*, 2008; Eyles *et al.*, 2009) aboard the twin *Solar Terrestrial Relations Observatory* (STEREO) spacecraft (Kaiser *et al.*, 2008). Coronagraphs and heliospheric imagers view the outward flow of density structures emanating from the Sun by observing Thomson-scattered sunlight from the free electrons in heliospheric plasma. This emission has an angular dependence which must be accounted for in the measured brightness (*e.g.*, Billings, 1966; Vourlidis and Howard, 2006).

Comparing coronagraph images of CMEs with heliospheric imager ICMEs has been difficult due to the separation between the outer limit of the coronagraph and the inner limit

of the heliospheric imager. For example, there is a gap of around $45 R_s$ ($\sim 30 \times 10^6$ km) between the outer edge of the LASCO field of view (FoV) and the inner edge of SMEI. Such comparisons have been attempted both on a case-by-case basis (e.g., Tappin *et al.*, 2004; Jackson *et al.*, 2006; Tappin, 2006; Howard *et al.*, 2007) and using statistical sampling (Howard *et al.*, 2006; Webb *et al.*, 2006, 2009; Howard and Simnett, 2008). From these studies it is clear that the greater the distance of the event from the Sun observed in SMEI, the more uncertain the association with LASCO events.

Data from the twin STEREO spacecraft are helping to overcome this problem. Its Sun–Earth Connection Coronal Heliospheric Investigation (SECCHI) instrument suite (Howard *et al.*, 2008) provides the means for continuous observations of CMEs from the Sun to Earth. SECCHI has a limited latitudinal FoV which SMEI overcomes by having all-sky imaging capability. Thus, SMEI and SECCHI are complementary instrument sets that together can be used to improve our understanding of CMEs/ICMEs.

Two primary science objectives of SECCHI are to determine the 3D properties of CMEs and the critical forces controlling their propagation in the corona and interplanetary medium. We are investigating the propagation characteristics of CMEs using data obtained by both the SECCHI imaging experiments and SMEI. In this paper, we present the first such comparison of a pair of events observed by LASCO, SMEI and SECCHI during January 2007. The scenario began as two major CMEs observed by LASCO that were less than a day apart, portions of which likely interacted, with possible merging as observed by the outermost instruments of SECCHI and farther out by SMEI. We discuss the effects of projection and mapping of each instrument and demonstrate how this combination of instruments provides a better picture of the CMEs/ICMEs than any single instrument alone. Finally, we discuss the physics behind the evolution of this set of events by comparing the data with four models: two kinematic, one MHD, and one a 3D reconstruction based on SMEI data (also involving kinematics).

2. The Instruments and Heliospheric Analysis Techniques

These events in January 2007 were observed by the Extreme ultra-violet Imaging Telescope (EIT) (Delaboudinière *et al.*, 1995) and LASCO, SMEI and the two SECCHI instrument suites. Both LASCO and EIT are on the SOHO spacecraft. LASCO consists of two operating coronagraphs, C2 with a FoV of $1.5–6 R_s$ and a cadence of ~ 30 minutes, and C3 with a FoV of $3.7–30 R_s$ and a cadence of ~ 50 minutes.

SMEI was launched in January 2003 into a dawn-dusk, Sun-synchronous, polar orbit at an altitude of 840 km. The SMEI sensor suite consists of three baffled CCD (charge-coupled detector) cameras, each covering a narrow $3^\circ \times 60^\circ$ strip of the sky. Camera 3 points nearest the Sun, Camera 2 is centered on the Earth's terminator, and Camera 1 points to the night sky. The cameras are mounted on the satellite with their FoVs aligned so that the FoV swath is a 3° wide strip extending 160° along an approximate great circle with the ends near the orbital axis. Since the satellite is zenith-nadir pointed, the combined FoVs of the cameras sweep out nearly 90% of the entire sky during each orbit. Gaps in coverage, or obscured areas, include a zone of exclusion of $\sim 20^\circ$ radius centered on the approximate sunward orbital pole, a smaller circle in the opposite direction, occasional areas shuttered due to sunlight in the sunward camera, particle enhancements from the polar zones and South Atlantic Anomaly, and a visible-light phenomenon associated with high-altitude geaurora. Most of the ICMEs observed by SMEI have been observed within $\sim 100^\circ$ elongation, or generally within about 1 AU (e.g., Howard *et al.*, 2006; Webb *et al.*, 2006; Howard and Simnett, 2008; Jackson *et al.*, 2008).

SECCHI has identical instrument suites aboard each STEREO spacecraft launched in October 2006. The SECCHI instruments on each spacecraft include an extreme ultra-violet full solar disk imager, two coronagraphs and two heliospheric imagers. The Extreme Ultra-Violet Imager (EUVI) obtains full disk solar images in four EUV wavelengths, producing images with a cadence as fast as 2.5 minutes in the most common wavelength (171 Å). There are two coronagraphs (CORs); COR1 has a FoV of 1.4–4.0 R_s and typical cadence of 8 min, and COR2 has a FoV of 2.5–15 R_s and cadence of 15 min.

Two Heliospheric Imagers (HIs) (Howard *et al.*, 2008; Eyles *et al.*, 2009) on each STEREO spacecraft view the inner heliosphere starting at an elongation of 4° from the Sun. HI-1 has a FoV of 20°, from 4–24° elongation (~ 12 –85 R_s), and HI-2 of 70°, from ~ 19 –89° elongation (~ 68 –216 R_s). There is a 5.3° overlap between the outer HI-1 and inner HI-2 FoVs. Unlike the EUVI and CORs, the HIs do not cover the entire position angle (PA) range around the Sun, but observe up to a 90° range in PA, usually centered on the ecliptic and viewing either east (HI-A) or west (HI-B) of the Sun. During the period of this study, STEREO was still being commissioned and the science operations phase did not start until April 2007. One consequence of this was that STEREO-A was rolled from solar north by 22.4° so that the HI FoVs were centered in the east-northeast rather than along the solar equator (see Figure 8 of Harrison *et al.*, 2008). For this study both HIs had an image cadence of two hours.

The STEREO spacecraft share similar ~ 1 AU orbits about the Sun as the Earth but separate from the Sun–Earth line by 22.5° per year. STEREO-A (Ahead) leads the Earth in its orbit, while STEREO-B (Behind) lags. In late January 2007 STEREO was only 3 months into its mission, so both spacecraft were still in close proximity to the Earth, only 0.5° apart. Thus, for the purposes of this study we assume that SOHO, *Coriolis* and both STEREO spacecraft were at the same location. As mentioned previously, during the time of this event, the STEREO spacecraft were not yet in their nominal observing attitudes, so that the images had a significant roll and translation associated with them. This has been accommodated for in the overlaid grids on the images.

As the images from each of the instruments are sky-plane projected, they do not directly provide information about the observed CME in the line-of-sight direction. Hence, the correct units to use for “distance” measurements are of elongation, the angle between the Sun–observer line and the vector from the observer through the point being measured (*i.e.*, the line-of-sight). Coronagraph measurements of distance are also originally in units of elongation and are then converted to distance, say in units of solar radii, with the application of various assumptions (*e.g.*, Howard *et al.*, 2007). Even in these cases the calculated values are skyplane-projected distances, and, therefore, give inaccurate estimates for a CME having a significant component along the Sun–Earth line. Methods to convert elongations to 3D distances have been discussed by Howard *et al.* (2007, 2008), Kahler and Webb (2007), Howard and Simnett (2008), and Wood *et al.* (2009). Heliospheric imagers also have projection effects due to the mapping to 2D images. SMEI images, for example, are typically shown in a Hammer-Aitoff projection (*e.g.*, Leighly, 1955) which is an equal-area mapping of a full 3D sphere. The analysis software for each SECCHI instrument provides the means to determine elongation angle and position angle (PA) for any point on an image. The PA for every instrument is set with its origin toward solar north and moving anticlockwise to complete a full 360° circle. We use heliocentric–ecliptic coordinates for the SMEI data and heliocentric coordinates for the SECCHI and SOHO data.

To illustrate the effects of elongation, consider a single point moving in the equatorial plane with a speed of 1000 km s⁻¹, as shown in Figure 1a (from Howard and Simnett, 2008). The elongation–time profiles shown are for the same point directed at different longitudes,

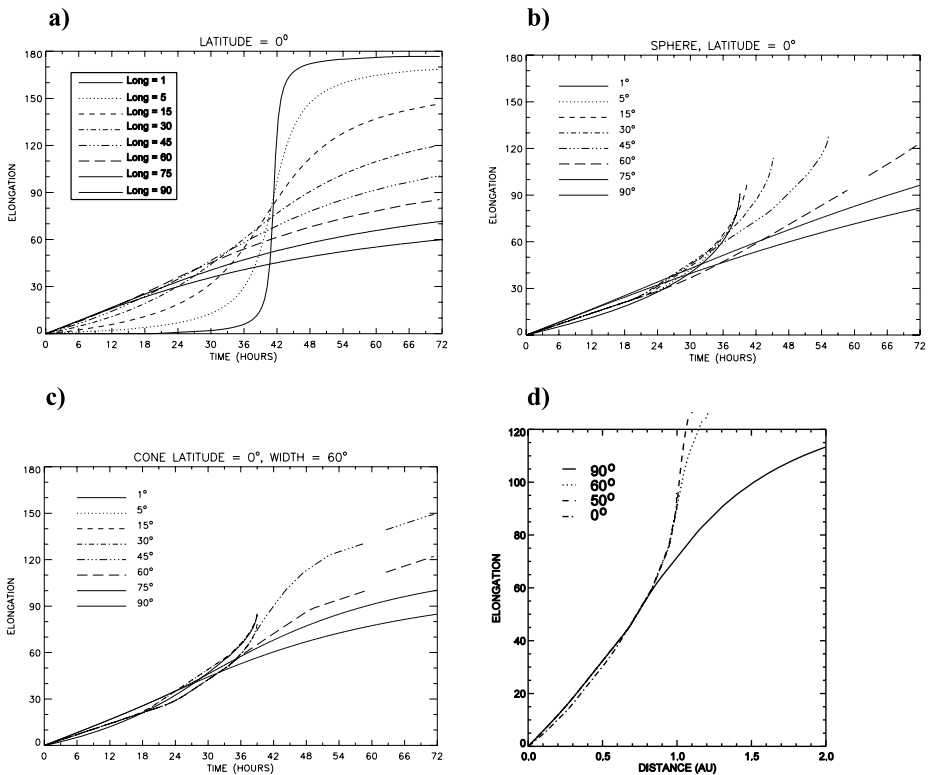


Figure 1 Elongation–time plots: (a) for a single point traveling with constant speed (1000 km s^{-1}) in the equatorial plane. We assume the point is launched at time $t = 0$. The curves represent the appearance of the elongation–time plot for the same points traveling in different longitudinal directions. 0° longitude represents the Sun–Earth line, or solar disk center, and 90° represents the solar limb. From Howard and Simnett (2008). (b) Elongation–time plots assuming that the shape of a CME is an expanding sphere, directed with the same direction and speed as the point from Figure 1a. (c) Elongation–time plots showing the same effect when the CME is an expanding shell of width 60° (the cone model). (d) Elongation vs. heliocentric distance plots for an ICME (modeled with a cone model of width 90°) moving with different directions from the Sun. Each curve represents a different trajectory, such that the central axis of the ICME is directed at 90° (along the solar limb), 60° , 50° , and 0° (the Sun–Earth line).

with 0° along the Sun–Earth line and 90° at the solar limb. Note that, although the curve is most distorted along the Sun–Earth line, those points nearest this line reach 90° elongation after about 40 hours, which is the time for a point traveling at 1000 km s^{-1} to reach 1 AU. Farther from the Sun–Earth line 90° elongation no longer indicates a distance of 1 AU, and so it takes longer for the point to reach this elongation value. Also note that none of the curves are linear, despite the apparent linearity of the distance–time profiles in heliospheric image data.

A further complication is that an ICME cannot be approximated as a single point. The ICME is a large structure, so that one may not always be observing the same part of the structure with each measurement. Howard and Tappin (2009) demonstrate, for example, that the apparent leading edge of an ICME changes as the ICME expands and moves outward, leading to an overestimate of its distance from the Sun based on the assumption that the same location on the ICME is being measured each time. Figure 1b shows the effect on an

elongation–time profile when one considers the shape of an ICME. In this case, the ICME is assumed to be an expanding sphere, moving in the same direction and speed as the point from Figure 1a. Figure 1c shows the same effect when the ICME is an expanding shell of width 60° (the cone model; *e.g.*, Zhao, Plunkett, and Liu, 2002; Michalek, Gopalswamy, and Yashiro, 2003; Xie, Ofman, and Lawrence, 2004). The main differences between these assumptions are that the elongation profiles are more closely approximated by a straight line, and do not change significantly in appearance as the direction of propagation changes. This information is useful for interpreting the propagation characteristics of ICMEs depending on their launch azimuth (or longitude) and shape or geometry as compared with actual data, such as we will show later.

Figure 1d shows plots of heliocentric distance (in AU) vs. elongation for the projection of an ICME of fixed dimensions (here a cone model of width 90°) moving at different directions from the Sun. The ICME with a central axis directed at 0° (the Sun–Earth line) impacts the observer at an elongation of 90° , so points beyond 90° are meaningless and excluded. The same is true for this ICME when directed at any angle up to 45° . The other variations show quite different conversion curves depending on the trajectory. The events close to the Sun–Earth line, for example, rise sharply in elongation with distance beyond about 1 AU. This procedure is similar to that resulting in Figure A2 of Kahler and Webb (2007) except that they assumed a narrow or compact ICME.

It should be noted that these effects become more significant at large elongations, beyond about 45° . Sunward of this distance, the Point P assumption (*e.g.*, Manoharan and Ananthakrishnan, 1990; Jackson, 1992; Howard *et al.*, 2006) is adequate (Section 3.2). Hence, Point P is appropriate for the coronagraphs, HI-1 and Camera 3 of SMEI (the innermost camera), but the more complex approach is required for Camera 2 of SMEI and HI-2. In the present paper we have taken this into consideration when converting between elongation angle and distance.

3. The Observations and Analysis

3.1. Overview of Events

Figure 2 illustrates the fields of view of the SECCHI and SMEI instruments. Figure 2a is a schematic showing the geometrical FoVs of the HI telescopes relative to the Sun and the Sun-centered COR2 coronagraph. The bottom scale is elongation east and west of the Sun, which is at 0° , at the center of the 8° diameter COR2 FoV. The elongation angle of the center of each HI telescope is shown, and their FoV ranges are given at the top. We note that, although this is shown as one flat diagram, the spacecraft are not co-located but widely spaced and separating with time. The dotted lines correspond to the square format of the HI CCD detectors, but the response in these corners is limited by optical vignetting. The optics for the HI-2s are optimized for a circular FoV, but on the sunward sides the corners of the FoV are completely obscured by the internal baffles, so the image is presented as a semi-circle on this side. On the sides away from the Sun the corners are affected by substantial vignetting. In addition, in the anti-Sun direction are two occulters meant to cover the bright Earth when the spacecraft were still near Earth during the early phases of the mission (see HI-2A image in Figure 2b).

The HI-A telescopes view to the east of the Sun-spacecraft line. Figure 2b shows an overlap view of the SECCHI-A telescopes together with an approximate scale in both solar radii and elongation, with the Sun on the right side at 0° . This image is a composite of

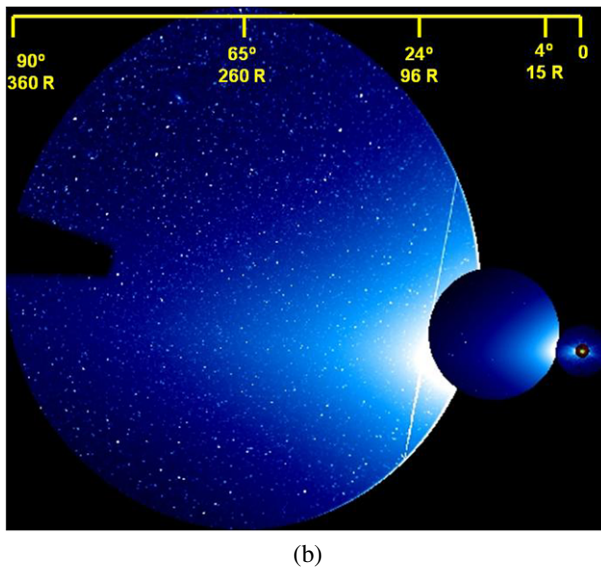
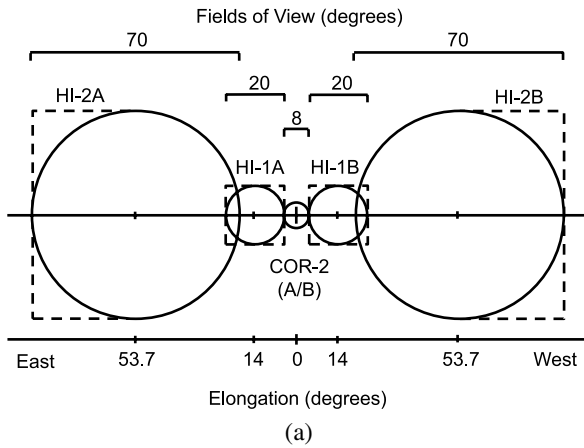
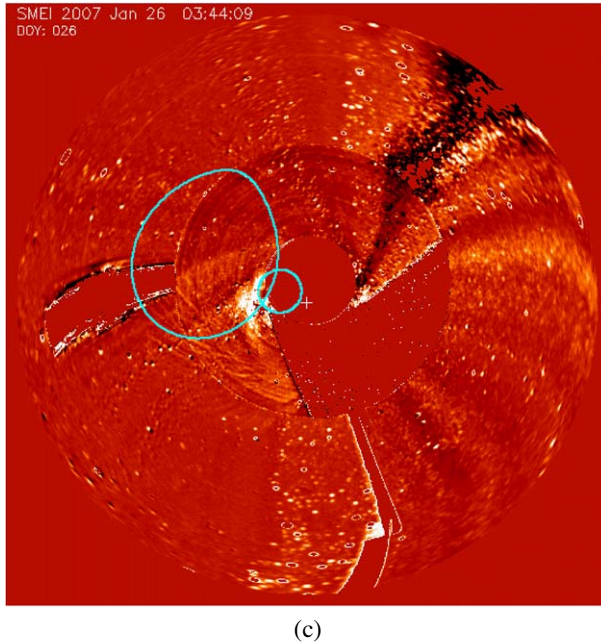


Figure 2 (a) The fields of view of the SECCHI HI telescopes and the COR-2 Sun-centered coronagraphs. The dotted lines correspond to the square format of the CCD detectors, although the response in these corners is limited by optical vignetting. The Sun-centered coronagraphs view all solar latitudes, while the HI FoVs are limited to a maximum of $\pm 35^\circ$ perpendicular to the ecliptic. From Eyles *et al.* (2009). (b) HI-A views east of Sun. An overlap view of all the HI-A telescopes together in early 2007 with an approximate scale in both solar radii and elongation (the Sun is to the right at 0°). Courtesy R. Howard. (c) HI-1A and HI-2A FoVs (blue circles) superposed onto a SMEI "fisheye" view on 26 January 2007. The normal HI circular FoVs become ovals in this projection format. The SMEI FoV extends to 135° elongation from the Sun, which is located at the + sign. The inner exclusion zone circle is 20° in radius. The Moon saturates the middle camera frames east of the Sun.

images taken during this period with the COR2, HI-1 and HI-2, right to left. Figure 2c shows a SMEI zenithal equidistant ("fisheye") image early on 26 January 2007. The ICME of interest is visible in the east-southeast quadrant. The HI-1A and HI-2A telescope FoVs (blue ovals) are superimposed onto the SMEI image. The SMEI FoV shown here extends to 135° elongation from the Sun, which is located at the + symbol. The inner exclusion zone circle



(c)

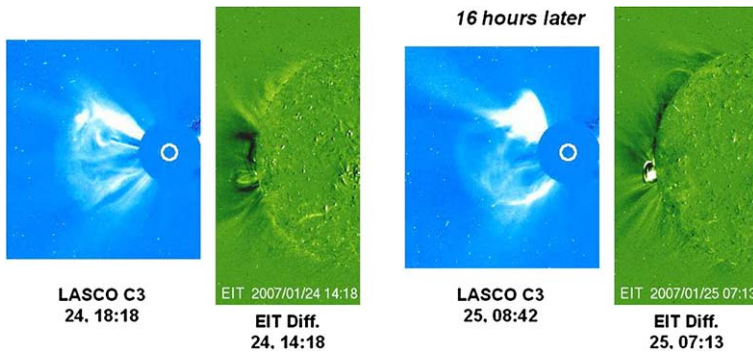
Figure 2 (Continued)

Figure 3 Example images of the two events on 24 and 25 January 2008 as observed by the LASCO C3 coronagraph and earlier at the east limb by EIT. The first event (left) was followed ~ 16 hours later by a similar but faster CME (right) from the same region. The EIT images are running differences. Note the bright arcade and the extended dimming region of the second event.

is 20° elongation in radius. The curved streaks to the southeast of the Sun are the vast tail of Comet McNaught (C/2006 P1) which extended out to near Earth (*e.g.*, Fulle *et al.*, 2007).

Figure 3 shows the events chosen for this study, as observed by LASCO C3 and the associated solar eruptions observed by EIT. Two similar CME events erupted over the eastern equatorial limb, with onset times about 16 hours apart. The first was associated with a GOES B9 X-ray flare with onset on 24 January at 13:45 UT and peak at 14:52 UT. Overall, the second event was more energetic, having an associated C6 flare ($S08^\circ E90^\circ$) with onset on 25 January at 06:33 UT and peak at 07:14 UT. The associated solar surface eruptions in

EIT suggest that the launch location of each CME was centered just south of the equator at the eastern solar limb. The events were first observed at EUV wavelengths on 24 January, 13:45 UT (in EUVI and EIT 195 Å images), and 25 January, ~05:48 UT, respectively (in EIT 195 Å images), and both had EUV waves (*e.g.*, Biesecker *et al.*, 2002) and extended dimming regions (*e.g.*, Thompson *et al.*, 2000). Both of these phenomena are considered good surface signatures of CME initiation. (See EIT running difference images in Figure 3. The EIT time on 24 January is a lower limit because no full-disk EIT images were taken before 13:42 UT due to a special-observations campaign. EUVI data were not available after ~10 UT on 25 January.) The coronal dimmings were also evident in the SECCHI COR1 images on both days (not shown), with the 25 January CME extending to the north. Harrison *et al.* (2008) noted that there was no reported active region on the eastern solar disk on 24 January, but that a new region (10940) had rotated into view at S06 latitude by 26 January. This region was likely associated with both of the CMEs.

Each event was well observed by LASCO, and the initial front, probably of the first CME, was observed by HI-1A from 24 January, 18:01 UT until 25 January, 04:01 UT. A 20-hour HI-A data gap through the end of 25 January prevented unambiguous detection of the second event; no HI-A data were available for most of 25 January. Starting on 26 January, at least five fronts were observed in HI-2A; these are indicated by the labeled arrows on Figure 4c. We identified as separate “fronts” only those features that had a discernable morphology that could be tracked over time. The first front, E0, was actually an arch-shaped feature, possibly two branches of a single loop. The second front, E1, faded after ~35° elongation while the third, E2, appeared to merge with the fourth, E3, at ~27 January at 02:00 UT. (These fronts as observed in HI-2A are hereafter labeled H2-0, H2-1, *etc.*) The merged structure continued to be visible until ~28 January, 06:00 UT, when it faded out at an elongation of 58°. We note that the HI observations of these events have also been discussed in papers by Harrison *et al.* (2008) and Lugaz *et al.* (2008).

Table 1 summarizes the onset times, location and derived speeds for each of the instrument sets. The combined LASCO C2+C3 speeds for the two events are listed in the CDAW catalog (http://cdaw.gsfc.nasa.gov/CME_list/) as 785 and 1367 km s⁻¹, respectively (other values from Harrison *et al.*, 2008 and Lugaz *et al.*, 2008 are also listed). The first CME is listed as having a PA width in LASCO of 147° whereas the second was an asymmetric halo, suggesting that a component of the CME structure was aimed Earthward. However, the brightest portions of both CMEs in LASCO had similar (PA) widths of 100° and 110° and were in or near the sky-plane. This is supported by the dimming regions in the EIT images that suggest the associated near-surface (“source”) region of both events was at the limb near the equator. The dimming region of the 25 January event was less evident on the EUV disk but extended farther north along the limb, and the bright arcade suggests that the CME axis was farther west in longitude (Figure 3).

SMEI observed at least three transient structures that could be tracked during this time period. The first feature, SMEI Event 1 (S1), appeared in Camera 3 about 21:00 UT on 25 January. It coincided in timing and appearance with HI-2A Event 1 (H2-1). Figure 4 (top) shows a side-by-side comparison of near-simultaneous scaled images of the main ICME from HI-2A (left) and SMEI (right). HI-2A is a difference image with each exposure of two hours duration. Note the similarities between the two images, particularly the bright ICME(s) and the tail fragments from Comet McNaught towards the south. We note that the ICME structure extended south of the HI-2A FoV, but the full structure was observed in SMEI. This demonstrates that HI and SMEI are complementary instruments and that combining measurements from each is important to understanding an event. The comet tail remnants, while obscuring some fine ICME structure during the transit of the ICME, provided an excellent fiducial for comparison between SMEI and HI-2A, demonstrating that

Table 1 Observational details of the January 2007 events.

Instrument	24 January		25 January		Reference
	Onset time, UT at height	Velocities (km s^{-1})	Onset time, UT at height	Velocities (km s^{-1})	
Location	(S06E90)		S08E90		
GOES	14:35		06:33		
EIT 195	< 14:18		05:48		
ST. COR1	14:03/1.5 R_s		06:43/1.5 R_s		Lugaz <i>et al.</i> (2008)
LASCO C2	14:23/1.5 R_s	623	06:54/1.5 R_s		NRL alert; Harrison <i>et al.</i> (2008)
LASCO C3	14:42/3.7 R_s	785/decel; 580; 600–750	07:42/3.7 R_s	1367/dcl; 1000–1350	CDAW(C2 + C3); Harrison <i>et al.</i> ; Lugaz <i>et al.</i>
ST. HI-1A	18:01/4.2°	604	–	–	Harrison <i>et al.</i>
ST. HI-2A	26,02:01/ 24.7°	(< 550)	–	–	Harrison <i>et al.</i>
Wind WAVES/ SWAVES	No type II? (data gap)		type II 06:55 ~ 11		

the same structure was observed by both instruments. See the online movies of the SMEI fisheye view for 25–29 January (M1) and of HI-2A for 24–28 January (M2).

Two additional ICME structures were observed only in SMEI Camera 2, since they were beyond the HI FoVs. SMEI Event 2 (S2) was visible starting at ~ 10 UT on 27 January and extending as a wide, outward-moving arc to the southeast that emerged from the comet tail obscuration. We later will propose two explanations for this structure: either it was part of a single loop from the 25 January LASCO CME, or it was part of the two merged ICMEs that was closer to the Earth. The last SMEI feature, Event 3 (S3), appeared as early as ~ 09 UT on 28 January as several faint, wide arcs to the north-northeast. Both of these events were detected beyond 80° elongation and outside of the HI-2A FoV. Most of the other elongation measurements, including the Camera 3 SMEI event, were made at $PA = 72^\circ$ while the latter two events were measured at 98° and 5° , respectively. For the second Camera 2 event, S3, a second measurement at 30° was also made.

3.2. Comparing SMEI and HI Images

As both HI and SMEI observe an overlapping region of the sky, we can compare images of the same region, as shown in Figure 2c early on 26 January 2007. While both SMEI and HI are centered in the ecliptic, the coordinate systems shown for each are different. For SMEI we used Heliocentric Earth Ecliptic (HEE) coordinates (*i.e.*, the equator is in the ecliptic plane) and for the HIs we used Heliocentric Earth Equatorial (HEEQ) coordinates (*i.e.*, the equator is the solar equator). All of the required information for obtaining the heliocentric coordinates is contained within the header file for each image, including the projection parameter and the spacecraft roll, pitch and yaw. Figure 5a and b show overlays of a heliocentric coordinate grid onto HI-1A and HI-2A images for the events in January 2007. Note that the zero latitude line, or ecliptic, is at a large angle to the horizontal because of the STEREO-A spacecraft roll angle noted earlier.

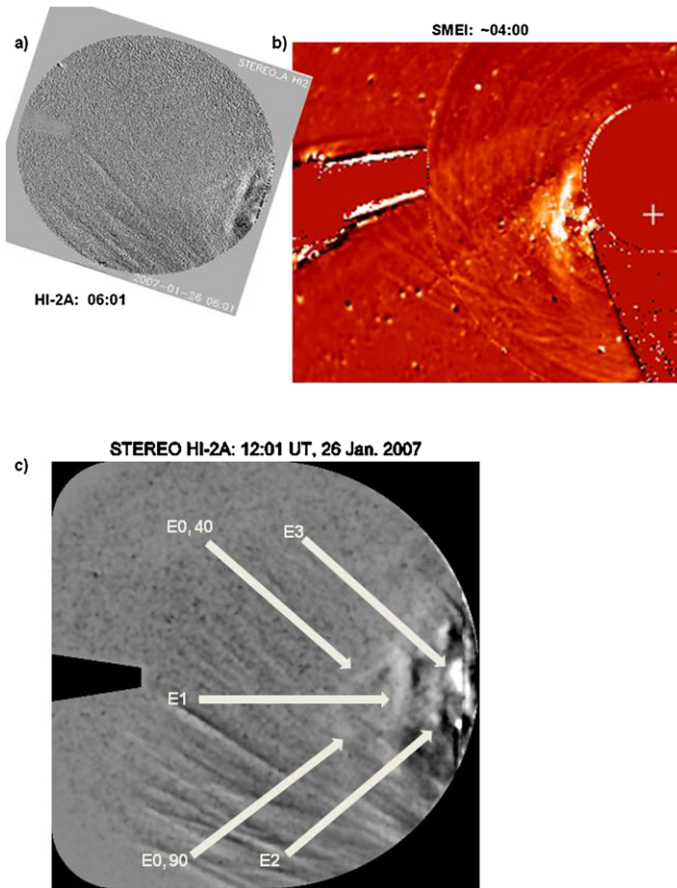


Figure 4 Comparison of near-simultaneous, scaled images of the January events from (a) HI-2A and (b) SMEI. The latter is a sub-image from the SMEI image in Figure 2c, which has the same HI-2A FoV (larger blue circle) superposed on it. HI-2A is a difference image; each exposure is 2 hours. The Sun lies 18.7° off the right edge of the HI-2A FoV, and its location in the SMEI image is marked by a + sign. SMEI is a direct image with a long baseline subtracted. At this distance of $\sim 30^\circ$, the orientation, shape and north–south dimension ($\sim 35^\circ$) of the ICME was the same in both imagers. Note the similarities between the two images, particularly of the ICME structure and the tail striations from Comet McNaught towards the south. The ICME material could be detected in both the HI-2A and SMEI Camera 3 images out to $\sim 35\text{--}40^\circ$. (c) Another HI-2A running difference image on 26 January at 12:01 UT. The arrows and labels indicate the five fronts discussed in this paper and tracked in Figure 6. HI-2A images courtesy of J. Davies.

Once the heliocentric coordinates have been established, the elongation can be determined from:

$$\cos(\varepsilon) = \cos(\Lambda) \cos(\Phi), \tag{1}$$

where Λ and Φ are the heliocentric latitude and longitude, respectively.

Likewise, the PA may be determined from:

$$\sin(\text{PA}) = 1 - \sin(\Lambda) / \sin(\varepsilon). \tag{2}$$

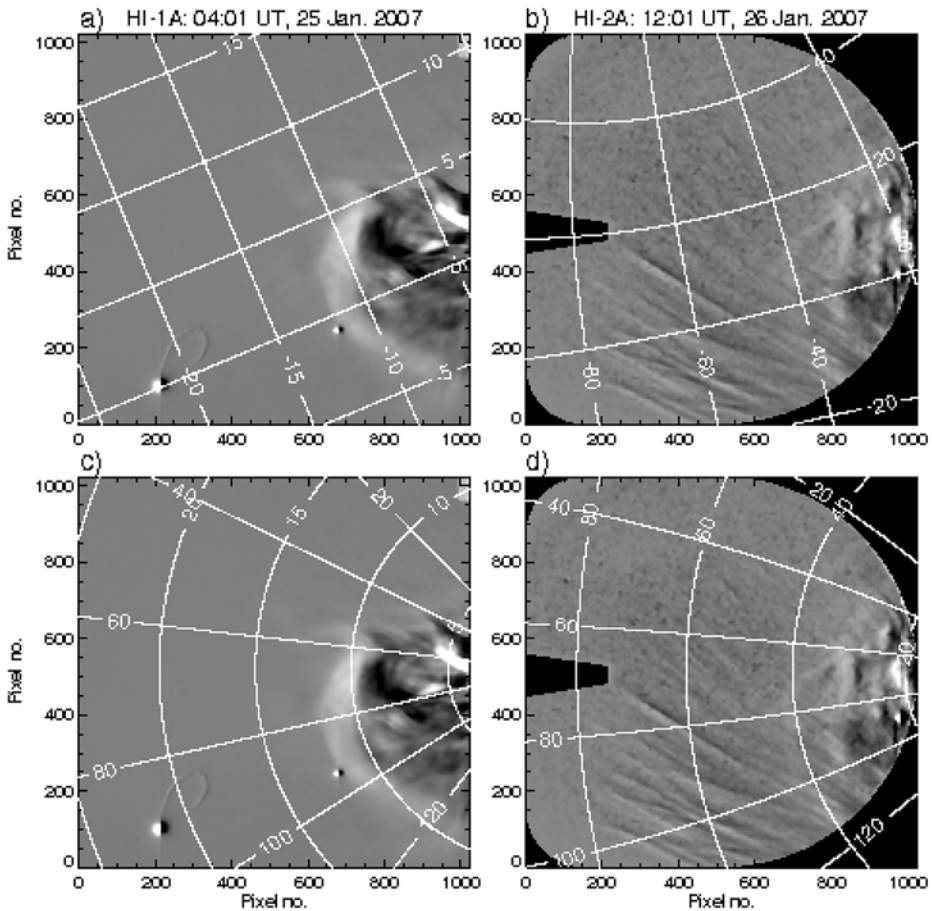


Figure 5 Overlays of heliocentric coordinate grids onto (a) HI-1A and (b) HI-2A images for the events in January 2007. Note that the zero latitude line, or solar equator, is at a large angle, because during this period the STEREO A spacecraft was undergoing a roll procedure. Overlays of elongation-position angle (PA) grids onto the same (c) HI-1A and (d) HI-2A images. The range of elongation and PA for each instrument is clearly shown. The orientations of the HI-1A and HI-2A FoVs are demonstrated in the three panels of Figure 2. Courtesy of J. Davies.

Figure 5c and d show overlays of an elongation-PA grid onto the same images as Figure 5a and b. Here the range of elongation and PA for each instrument is clearly shown, although the PA range is different from what is now typical of the HIs again because of the large spacecraft roll angle during this period.

Once the elongation and PA have been established, the distance can be determined in the same manner as for SMEI. It must be noted that elongation angle is always measured relative to the observer–Sun line, which for the STEREOs is different from the Sun–Earth line. For measurements early in the mission such as the events here, the differences are negligible, but become more significant as the spacecraft move farther from Earth. Thus, the angular difference between the Earth and the spacecraft needs to be accounted for, although the geometry will remain the same.

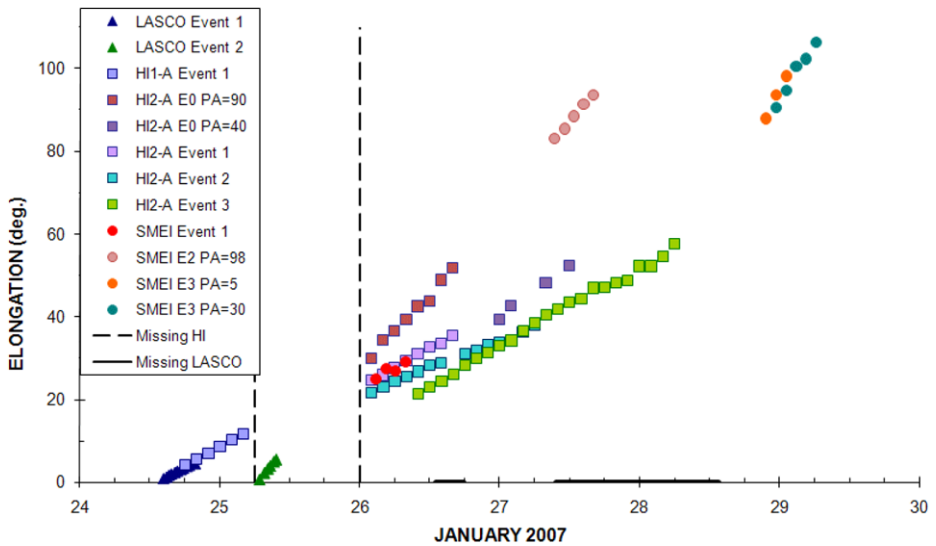


Figure 6 Elongation–time plots of CME fronts observed from 24–30 January 2007 by LASCO, SMEI, and the HIs. The shapes and colors of data points denote experiment and ecliptic PA measurements of each measurement: LASCO–triangles, HI’s – squares, and SMEI – circles. The vertical dashed lines denote the HI data gap.

4. Results

4.1. Kinematic Evolution – Data

Figure 6 shows elongation–time plots for the two LASCO fronts (triangles), the five HI fronts (squares), and the three SMEI features (circles). It shows elongation–time plots for all our measurements from each instrument, with periods of missing HI and LASCO data also noted. All of the measurements without a “PA” label were measured at the same PA of 72° . As discussed later, the northern- and southern-moving branches of the leading HI-2A Event 0 (H2-0) were measured at PAs of 90° and 40° , respectively. Finally, the large-elongation SMEI fronts called S2 (to the east-southeast) and S3 (to the north-northeast) were measured at PAs of 98° and 5° and 30° , respectively. Two PAs were measured for S3 because the arc was faint and difficult to track due to particle obscuration.

The HI data gap makes distinguishing separate events difficult, especially during a period when the faster, later LASCO CME may have passed and/or interacted with the first CME. There was an apparent superposition of two structures (E2 and E3 = H2-2 and H2-3) within the HI-2A FoV at ~ 12 UT on 26 January. Although some interaction or merging between the two CMEs was possible, our observations suggest that at least portions of the original events continued outwards as separate structures with unvarying kinematics.

The elongation–time plots for LASCO/HI-1A Event 1 (L_1 and H1-1) matched well and appear to continue after the HI data gap as SMEI/HI-2A Event 1 (S1 and H2-1). The trailing H2-2 and H2-3 events appeared to merge and then continue toward the later S3 observed on 28–29 January. We confirmed that our track for Event 1 is nearly identical to that of front “A” in Harrison *et al.* (2008) (see their Figure 15) and, therefore, that this feature is the same one that they discuss. Their measurements for this front were made at a PA of 68° , whereas ours discussed so far were made at 72° .

The second, faster LASCO Event 2 (L_2) occurred during the HI data gap and was not clearly discernable in HI-1A. However, the elongation–time plot of the southern branch of the leading arch-shaped structure observed in HI-2A, which we call E0, PA = 90, appears to lie along a track connecting the earlier LASCO CME and later SMEI S2. These had similar trajectories, with H2-0 measured at 90° and S2 at 98° in PA. We also measured the northern branch of the arch-shaped structure, which we call E0, PA = 40, at a PA of 40° and find that it appeared to be associated with the slower HI-2A structures and possibly with the northern S3.

4.2. Physical Evolution – Modeling

The kinematic measurements in Figure 6 are in units of elongation, as (discussed earlier) this is most meaningful “distance” measurement using heliospheric imagers. To convert elongation to distance, it is essential to combine the mapping effects with the geometry of the ICME relative to the observer. Howard and Tappin (2009) have established the theoretical framework for this procedure by combining the brightness of the ICME due to the effects of Thomson scattering with the effects of changes in ICME geometry and trajectory.

4.2.1. Drive-Drag Model

We have modeled the kinematic evolution of both LASCO events in two ways, first for the drag situation where each ICME decelerates to the solar wind speed, and second where a driving force is included. This combination was used by Howard *et al.* (2007) and is effectively a modification of the ICME Lorentz force imposed by Chen (1996) with the more realistic drag force of Tappin (2006). The former is represented by the following equation:

$$\frac{d^2 R}{dt^2} = \frac{I_t^2 \ell}{c^2 R M} \left[\ln \left(\frac{8R}{a} \right) - \frac{1}{2} \frac{B_t^2}{B_{pa}^2} - 1 + \frac{\xi}{2} \right], \tag{3}$$

where I_t and B_t are the toroidal current and magnetic field respectively, B_{pa} is the poloidal magnetic field at a , ξ is the internal inductance of the flux rope, ℓ is the length of the flux rope, and R is its major radius. Chen (1996) imposed a simple drag force to this model, but we include a more sophisticated drag force, discussed by Tappin (2006) and represented by a pair of coupled differential equations:

$$\begin{aligned} \frac{d^2 R}{dt^2} &= -\frac{dM}{dt} \frac{v_c(R) - v_{sw}(R)}{M(t)}, \\ \frac{dM}{dt} &= \Omega \sigma(R) (v_c(R) - v_{sw}(R)), \end{aligned} \tag{4}$$

where M is the mass, v_c and v_{sw} are the ICME and solar wind speed, respectively, σ is the solar wind sector density, and Ω is the heliospheric solid angle of the ICME. We consider two situations: *i*) the CME decelerates only according to the drag force, and *ii*) the net acceleration is the combination of the Lorentz force in Equation (3) and the drag force in Equations (4). We note that Tappin (2006) also utilized the drag force of Cargill (2004). However, given that there is little difference between this drag and the snowplow drag described in Equations (4) within 1 AU, we used only the snowplow drag in the present study.

The result of this model is a distance–time plot derived from the input parameters of the ICMEs shown in Table 1 and mass estimates of 4.3×10^{15} g and 1.6×10^{16} g for LASCO

Events 1 and 2, respectively. The initial excess mass of the CME was determined from the standard technique for mass calculation in the LASCO software (*e.g.*, Vourlidas *et al.*, 2000). This makes use of Thomson scattering physics to convert the intensity of a given area on a LASCO image to mass. We note that the excess mass calculated using a pre-event background-subtracted LASCO image is the mass of the CME above the background level, *i.e.*, above the value of the ambient solar wind. However, following Tappin (2006) and Howard *et al.* (2007), in our simple calculation we have assumed that the total mass is equal to the excess CME mass (obtained from LASCO) plus the solar wind mass, since most or all of the mass is likely transported out.

Using the geometry considerations discussed in Section 2, we performed a conversion from distance to elongation assuming the ICME structure can be modeled as a cone of width 100° and 110° for Events 1 and 2, respectively. Each was assumed to have its central axis in the equatorial plane on the eastern solar limb.

Figures 7a and b show the data from Figure 6 with the results from the model superimposed. The results for both the 24 and 25 January LASCO CMEs and applying drag only (D) and driving + drag (A + D) components of the model are shown as the colored curves. Figure 7a shows the results assuming the Point P approximation used by Howard *et al.* (2006), and Figure 7b shows the results using the cone model discussed earlier. It appears that the Point P measurements better match the drag or deceleration model alone for the first L_1 event, where the curve lies just above the SMEI Camera 3 and HI data points, and then continues toward S3 on 29 January. L_2 appears to be better represented by the cone model in Figure 7b, where the S2 event points on 27 January lie between the deceleration and drive + drag models for this event. The best match for both the H2-0 (PA = 90°) and S2 data appears to be with the drag-only model.

4.2.2. HAFv2 Model

In addition, we also ran the Hakamada–Akasofu–Fry Version 2 (HAFv2) 3D solar wind kinematic model (Hakamada and Akasofu, 1982; Fry *et al.*, 2001, 2003) for comparison with the SMEI and HI observations for the January 2007 events. The HAFv2 model is a kinematic model that predicts solar wind conditions at Earth and elsewhere in the solar system based on observations at the Sun. The model projects fluid parcels outward from 2.5 or 5.0 R_s from the Sun to beyond 100 AU along fixed radials at successive time steps, in an inertial frame. The parcels move outward with different speeds along fixed radials as the Sun rotates beneath the grid and the solar magnetic field is carried outward with the solar wind flow.

The HAFv2 model uses two sets of inputs. The first set establishes the steady-state boundary conditions for the background solar wind, and the second set determines the time-dependent boundary conditions for the event-driven (transient or interacting) solar wind. The HAFv2 model uses source surface maps derived from synoptic solar observations, typically from the WSA model (Wang–Sheeley–Arge; *e.g.*, Arge and Pizzo, 2000) to establish the background solar wind conditions. It is also driven by observational proxies for the energy released during solar events to model CMEs and interplanetary shock propagation. The HAFv2 model has been used in several recent studies for comparison with SMEI observations to better understand the kinematics of ICME propagation. The most basic output of the HAF model are ecliptic plane projections of propagating shock waves, which can then be used to derive distance–time or elongation–time plots of the fronts of these structures. Kinematic studies have been done comparing SMEI and HAFv2 for several events (Howard *et al.*, 2007; Sun *et al.*, 2008;

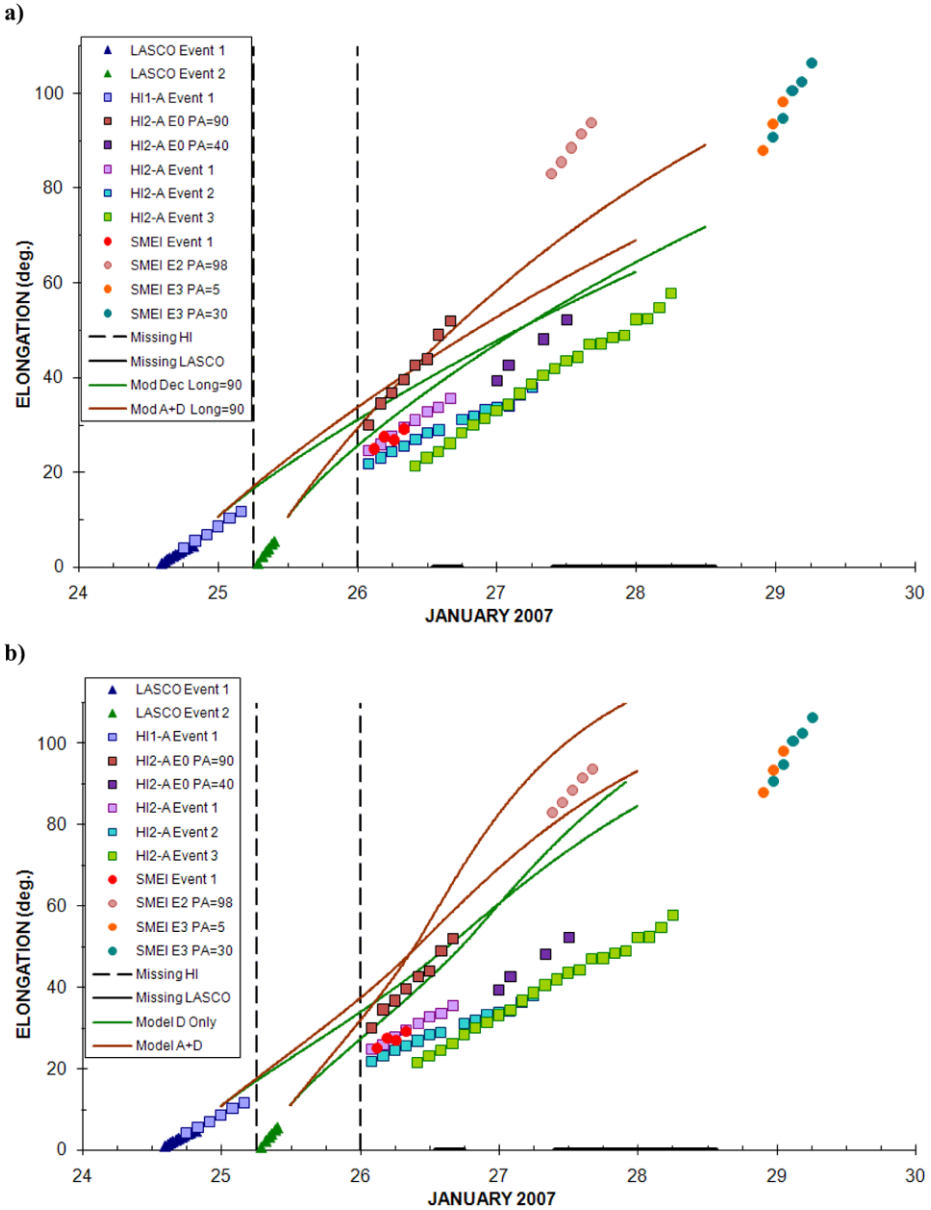


Figure 7 Comparison of four model runs with the same elongation – time data of Figure 6. For (a) and (b) the resultant colored lines for each event for drag only or driving + drag are superimposed on the data of Figure 6. (a) Elongation – time curves assuming the Point P approximation and that the material is launched at 90° or at the east limb. (b) Elongation – time plots assuming each ICME can be approximated by a cone, symmetric about the equatorial plane, with longitudinal width the equivalent of latitudinal width. (c) Elongation – time curves of the ICMEs run with HAFV2 in the ecliptic plane. Merging of the two events is apparent on 26 January at an elongation ~ 30°. (d) Elongation – time curves of the two fronts for the ENLIL model, again in the ecliptic plane. As with the HAFV2 results, merging of the two events is clearly visible, also on 26 January, only this time at an elongation of ~ 45°.

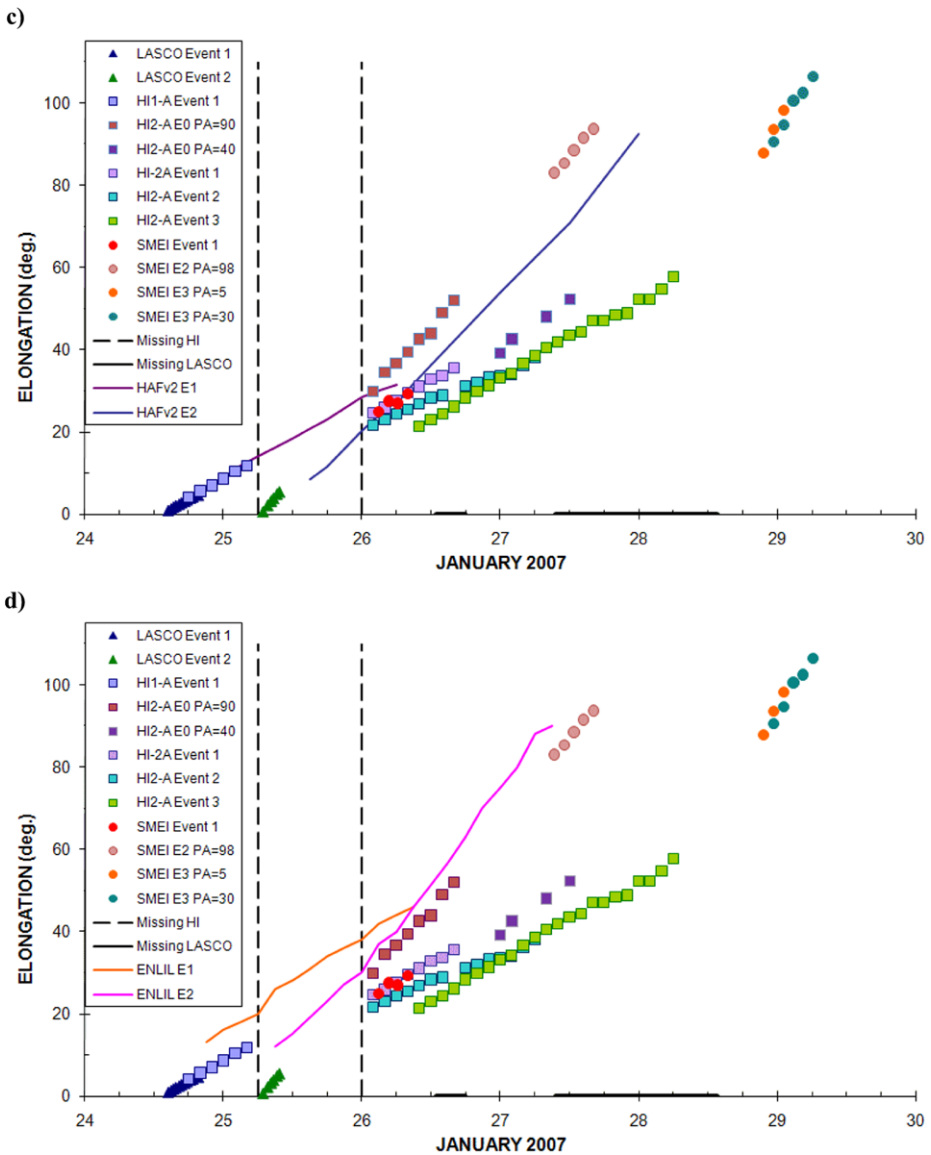


Figure 7 (Continued.)

Jackson *et al.*, 2008), and the SMEI images have confirmed that the HAFv2 simulations of the ICME geometry are reasonably accurate. Here we use only the ecliptic-plane, distance–time data from the HAF model for comparison with the SMEI observations and an MHD model (see later).

Figures 8a and b show two snapshots of the HAFv2 simulations of the ecliptic plane IMF during the January 2007 event period. These show the IMF in the ecliptic plane out to 2 AU with the locations of the inner planets marked. Earth is on the 1 AU circle. The magnetic polarity of the spiral field lines are marked as red or blue. The Air Force Weather

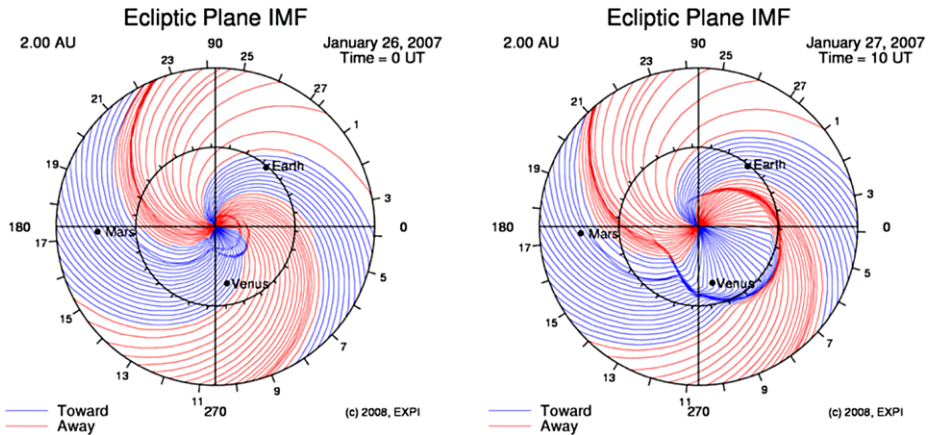


Figure 8 Snapshots of the WSA-HAF v2 model run showing the propagation of the two shocks (a – left) on 26 January at ~ 00 UT and (b – right) after merging on 27 January at ~ 10 UT. These show the IMF in the ecliptic plane out to 2 AU with the locations of the inner planets marked. The magnetic polarity of the spiral field lines are marked: red = away and blue = toward the Sun.

Agency issued forecasts several hours after the onset of each of the disturbances observed on 24 and 25 January, based on HAFv2 simulations of the interplanetary response to the solar eruptions. These are a continuation of the Fearless Forecast study of real-time predictions of interplanetary shock arrival time (SAT) at Earth (*e.g.*, Fry *et al.*, 2003). The RMS error in SAT predicted by HAFv2 for more than 340 events during 1997–2002 was ~ 12 hrs (Fry *et al.*, 2003; McKenna-Lawlor *et al.*, 2006). For the January 2007 events, the second shock was predicted to overtake and merge with the first, with the combined shock arriving at Earth at 00 UT on 28 January. A very weak shock was observed in ACE data at 04 UT on the 28th, approximately 4 hours after predicted.

The solar disturbances were initiated using essentially the event characteristics listed in Table 1, namely onset time, source location, and initial speed. The HAFv2 model also requires that an exponential rise/decay time constant be specified to characterize the evolution of the velocity pulse imposed upon the inner boundary (see McKenna-Lawlor *et al.*, 2006 for details). The time constants associated with the two CMEs were selected to be 1 hour and 5.5 hours, respectively, based upon the observed GOES X-ray temporal profiles. The HAFv2 simulation shows, in Figure 8a on 26 January at 00 UT, two interplanetary shocks driven by the events on the 24 and 25 January moving outward from the Sun's east limb. A time sequence of the ecliptic plane plots indicated that by 26 January, 12 UT, the two shocks had merged at a distance of ~ 0.5 AU from the Sun. Figure 8b for 27 January at 10 UT shows that the two shocks had merged and moved beyond 1 AU.

Figure 7c shows the HAFv2 elongation–time curves of the ICME in the ecliptic plane overplotted on the original data for this period. The merger of the two events is apparent on 26 January at an elongation $\sim 30^\circ$. As with the drive-drag model, it seems the HAFv2 projection of the first L_1 event aligns with the HI and SMEI Camera 3 data throughout 26 and 27 January, which is then matched through the data trend with S3 on 29 January. The faster L_2 event overlaps the early segments of the HI-2A and SMEI data, but trends along with the H2-0 (PA = 90) points toward S2 on 27 January. We note that the HAFv2 fit for the second event appears to be a few hours ahead of the LASCO data.

4.2.3. MHD Model (ENLIL)

ENLIL is 3D, time-dependent, magnetohydrodynamic (MHD) model (e.g., Odstrcil *et al.*, 2003) which is able to compute dynamic interactions in the inner- and mid-heliosphere, provided that time-dependent boundary conditions are specified at $21.5 R_s$ (0.1 AU), well outside the sonic point. It is based on the ideal MHD equations that are solved by an explicit finite-volume scheme. It solves for plasma mass, momentum, energy density, and magnetic field. The outer boundary is adjustable. It has a well-defined and documented interface and has been adapted to work with other time-dependent numerical solar MHD codes (e.g., Odstrcil *et al.*, 2004). The ambient or background solar wind can also be input at the base from other “full-rotation” models (e.g., Bisi *et al.*, 2008). The runs for this period, Carrington Rotation 2052, were driven by the current version of the WSA empirical model (Arge and Pizzo, 2000) of radial magnetic fields and velocity.

Transient disturbances are simulated in ENLIL by launching an over-pressured plasma cloud. This simulates coronal ejecta and, depending on conditions, an interplanetary shock can be generated. ENLIL can differentiate between post-shock and ejecta density. (The HAF model specifies a shock with some duration of post-shock parameters, but does not simulate ejecta *per se*.) The location, size and velocity of such ejecta can be derived by fitting coronagraph observations with, for example, the cone model. The plasma shape is currently launched as a spherical homogeneous structure, although it can be elongated to simulate long-duration events, and then becomes distorted as it encounters the background heliospheric structures.

The launch times used for the ENLIL run were 24 January at 19:00 UT and 25 January at 09:25 UT with initial speeds of 780 and 1300 km s⁻¹. These values were used to correspond with the LASCO C3 observations of the CME fronts at $21.5 R_s$, the inner boundary of the ENLIL model. The launch locations used for both events were S05°E90° and CME widths of 100° and 120° measured from the LASCO C3 images were input for the shape of the plasma ejecta.

Figure 9 shows two snapshots of the WSA-ENLIL-Cone model run for the January 2007 events at about the same times and positions as for the HAF model in Figure 8. The CR2052 synoptic magnetic field data used were from the National Solar Observatory. The ENLIL outputs show density according to the color scale in the ecliptic plane (left), and in a meridional cut through along the east limb (right; longitude = -90°). The radial distance extends to 2.5 AU, and Earth’s location is the yellow disk on the 1 AU circle. See the online Movie M3 of the ENLIL run for this period.

Figure 7d shows elongation–time profiles of the two fronts for the ENLIL results, again in the equatorial plane. As with the HAFv2 results, the merger of the two events is clearly visible, also on 26 January, only this time the model predicts it to occur at an elongation of ~45°. As with HAFv2, it appears the first L₁ event matches best with the trend of the SMEI Camera 3 and HI data, while the faster L₂ event matches with the H2-0 (PA = 90) points and the S2 data on 27 January. Note that the onset times for both ENLIL simulations appear to be misaligned with the LASCO data. This is because the onset times of the LASCO CMEs were assumed to coincide with the times when their leading edges passed the lower boundary of the ENLIL model. If we were to adjust these onset times to agree better with, say, the HAF curves, then the matching of the model curves and data points for Events 1 and 2 as described above would be duplicated by ENLIL.

Since the 3D ENLIL results can be viewed in any plane, we produced a movie simulating the same view as the SMEI fisheye projection (online Movie M4). In this simulation total white-light brightness maps are produced by integrating the model output densities along

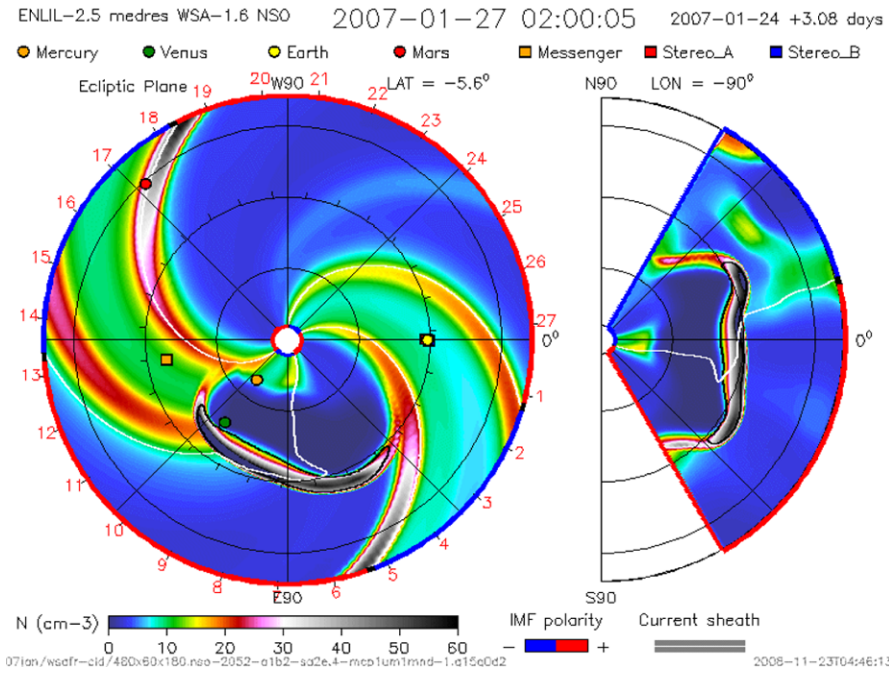
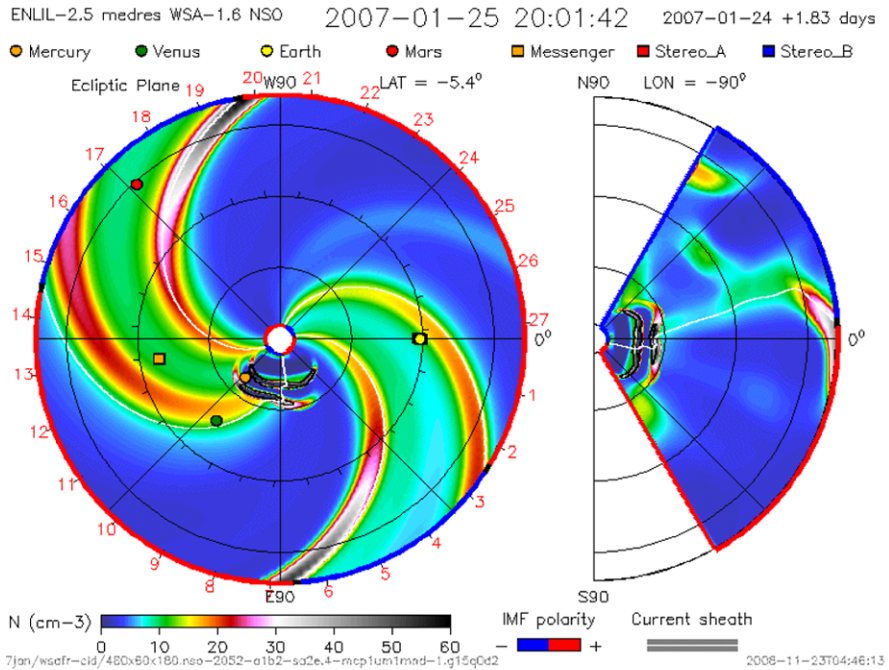


Figure 9 Snapshots of the WSA-ENLIL-Cone model run for the January events at similar times and positions as shown for the HAF run in Figure 8. These show density according to the color scale in the ecliptic plane (left), and in a meridional cut along the east limb (right; longitude = -90°); note the extended features to the north (top) and south (bottom). The Earth’s location is the yellow circle. The IMF polarity is shown in red (+ or away) or blue (- or toward) on the outer boundary circle.

lines of sight from Earth, taking into account Thomson-scattering effects. A single frame is shown in Figure 10c depicting the Sun-centered view from Earth out to 90° elongation (left) for the ENLIL density data shown in the ecliptic plane view (similar to Figure 9) on the right. Elongation lines every 10° emanating from Earth are drawn. We see that a broad arc at $40\text{--}50^\circ$ results when integrating through the dense ICME shell that is extended in both the longitudinal and east limb meridional (Figure 9, right) directions. For comparison Figure 10a shows the east-southeast quadrant of the SMEI fisheye view on 27 January at ~ 17 UT. The arrow points to the moving arc which we call S2 as plotted in Figure 6 (see online Movie 1). Figure 10b is a 3D reconstruction fisheye view of the SMEI data (see next section) at about the same time showing the loop also extending to the north. Although certain areas of the SMEI images (and reconstructions) are obscured by the Moon, orbital particles and the comet tail, the similarity of at least the east–southeast portion of the arc with the ENLIL simulation is remarkable.

Lugaz *et al.* (2008) discuss the results of a similar MHD simulation of these January events using the Space Weather Modeling Framework (SWMF) codes. One important difference between that simulation and our ENLIL simulation is that Lugaz *et al.* use a flux rope to model the CME ejecta (see Lugaz *et al.*, 2007). They emphasize comparison of the HI-2A image and simulation early on 26 January, finding that their simulated structures match those in HI-2A and that the two leading structures in HI-2A are the 24 and the overtaking 25 January CMEs, respectively. However, our interpretation differs in that our more complete data set and modeling suggests that by the time after the HI data gap, the faster LASCO event has already overtaken and passed the 24 January CME.

4.2.4. SMEI 3D Event Reconstruction

At the Center for Astrophysics and Space Sciences at the University of California, San Diego (UCSD), the SMEI data are processed to retain their inherent photometric precision. Two data products are now routinely produced at UCSD: *i*) all-sky maps consisting of photospheric sunlight Thomson-scattered from heliospheric electrons, from which stellar and zodiacal-light backgrounds have been removed (*e.g.* Buffington *et al.*, 2007; Hick, Buffington, and Jackson, 2007), and *ii*) 3D tomographic reconstructions which use the sky maps as input and from which are removed geo-auroral light (*e.g.* Jackson *et al.*, 2006, 2008; Bisi *et al.*, 2008). These SMEI data products, the sky maps, sky-map differences and 3D-reconstruction images, for the entire SMEI data set are now available for public viewing and downloading at: <http://smei.ucsd.edu/>. Details on the UCSD processing are discussed in Jackson *et al.* (2004, 2006, 2008), and Hick, Buffington, and Jackson (2005, 2007).

Briefly, the sky map processing begins by combining all the 4-second data images into sidereal-coordinate all-sky maps. The final sky maps have had rapidly-varying sources of noise, such as high-energy-particle hits removed, and the zodiacal background removed by the subtraction of a model, which also removes most long-duration, solar PA-dependent and annually varying backgrounds. The 3D reconstructions begin with fitting of a heliospheric model to the SMEI-observed brightness, using the Thomson-scattering parameters of Billings (1966). Since interplanetary scintillation (IPS) velocities were not available during this January period to provide 3D-structure determinations, we used a constant velocity (400 km s^{-1}) to convert the SMEI-observed brightness to density. Data are then extracted from the sky maps at sidereal locations having $\sim 5^\circ$ centers binned to $1^\circ \times 1^\circ$, and the geo-auroral light removed. The accuracy of the density structures revealed by the SMEI 3D reconstructions can be tested by comparisons with the *in situ* densities observed by near-Earth spacecraft, *e.g.*, Wind or ACE, and now by the STEREO spacecraft, in the ecliptic (*e.g.*, Jackson *et al.*, 2008).

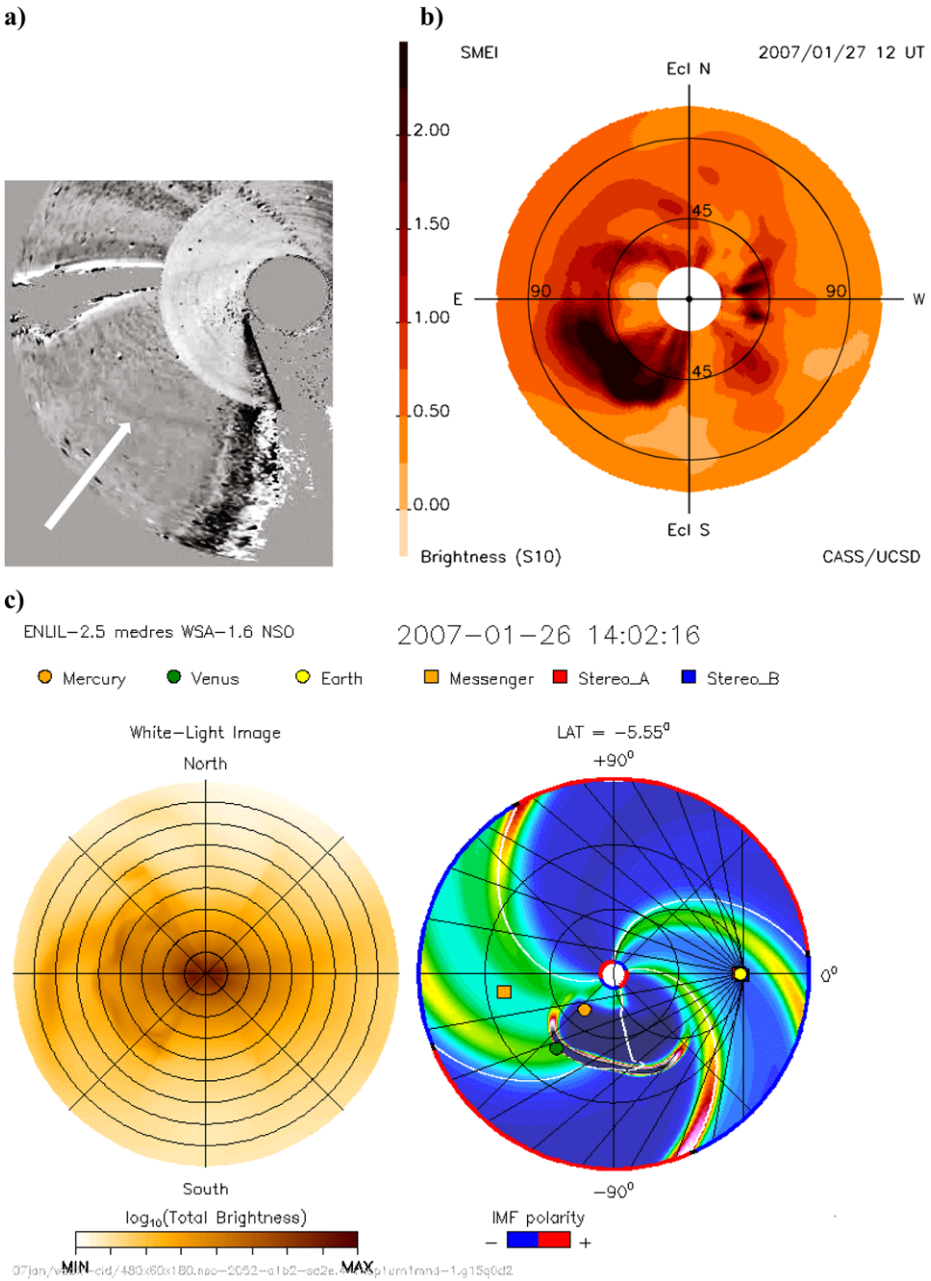


Figure 10 (a) View of southeast quadrant of SMEI fisheye image on 27 January at ~17 UT showing long loop (S2 – arrow). The image is similar to the earlier one of Figure 2c, but in reversed gray scale to show the faint structure. (b) A 3D reconstruction fisheye view of the SMEI data at about the same time showing dense material associated with the same loop which also seems to extend to the north. (c) ENLIL frame showing the merged front to the east in total brightness at about the same elongation as the SMEI images. (d) The ecliptic plane view from ENLIL. Compare with the SMEI loop and compare the online movies. Although certain areas of the SMEI images (and reconstructions) are obscured by the Moon, orbital particles and the comet tail, the similarity of the observed arc(s) with the ENLIL simulation is remarkable.

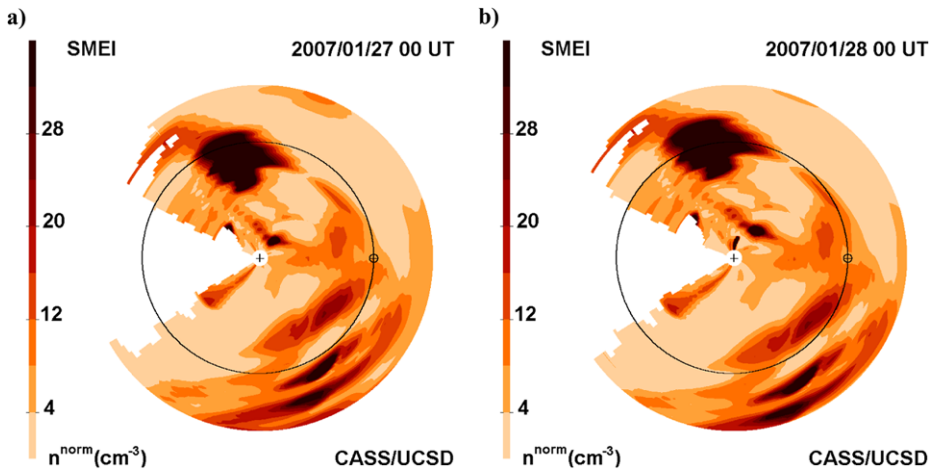


Figure 11 A pair of images, on 27 and 28 January 2007, both at ~ 00 UT displaying the changing density in the ecliptic plane as extracted from the SMEI 3D tomographic reconstruction of this time period. The Sun is at the center noted by the + sign, and the Earth is given by its symbol \oplus along with a black circle at 1 AU distance mapping the Earth's orbit about the Sun in the ecliptic. Note that darker shades of color represent higher density values. There were a number of ICMEs during this period, but the one likely associated with S2 passes Earth's orbit east of the Earth on 28 January at ~ 00 UT. Also, we reconstruct what we think is comet tail material out ahead of the CME due to the presence of the bright Comet McNaught tail to the east in the SMEI all-sky images.

We performed a 3D reconstruction analysis of the heliospheric density from SMEI in late January 2007. A movie shows the evolution of the 3D density structure as projected in the ecliptic plane for a 2-week period that includes the January events. Figure 11 presents a pair of snapshot images from the movie, on 27 and 28 January, both at 00 UT. The Sun is at the center and Earth is shown on the ~ 1 AU circle. The density has been normalized by $1/R^2$ to highlight the faint heliospheric structures (darker shades of color represent higher densities). The SMEI 3D reconstruction reveals interconnected global structures that are not clear in the SMEI quick-look processing. The reconstruction suggests that there were a number of probable ICMEs during this period. One feature is the broad, dense structure that passed the Earth's orbit to the east of Earth on 28 January. We believe there was material from the bright Comet McNaught tail to the east and possibly co-mingled with this ICME. The elongation–time position of this ICME seems to match that of S2 (see Figures 6 and 10).

Because the ICME loop observed in the SMEI data (Figure 10 top) extended south of the ecliptic plane and the Moon saturated Camera 2 to the east, we produced slices through the same 3D density reconstruction data set as with Figure 11, but displayed in planes tilted 30° and 45° southeast–northwest from the ecliptic plane. Figure 12 shows these views in two snapshots at 27 January, ~ 00 UT. As expected, in these planes the ICME loop structures appear to be denser, although the comet tail dust and plasma are still present since they also extend to the south.

4.2.5. Conclusion from Data–Model Comparisons

Based on the results from the comparison of the data with each of these models, it seems likely that it is the first LASCO event that is associated with the SMEI and HI events through 26–28 January, which then became the northeast SMEI event on 28–29 January. The faster

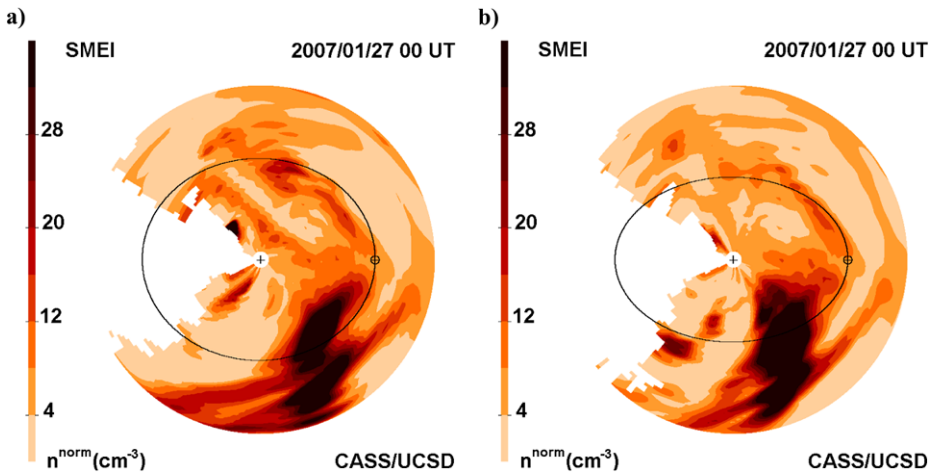


Figure 12 Images from the same SMEI 3D density reconstruction data as in Figure 11 but displayed in planes tilted 30° (left) and 45° (right) southeast–northwest from the ecliptic plane. The images are both for 27 January at 00 UT. In these planes the ICME loop structures are denser and more easily distinguished from the comet tail dust and plasma.

L_2 event was faintly detected by HI-2A after the data gap and likely became the east–southeast event detected as S2 (Camera 2) on 27 January. It remains unclear whether merging occurred between these two events, although the HAF and ENLIL models reveal clear merging of the fronts. The 3D reconstructions help in this regard: Although in the ecliptic plane there appears to be one structure similar to the HAF and ENLIL runs (Figure 11) therefore implying merging, the fisheye data (Figure 10) suggest that at least portions of the two events continued as separate loop structures as far out as 1 AU.

Lugaz *et al.* (2008) conclude that the brightest front visible in HI-2A (and in SMEI – see Figure 4) is the faster second LASCO CME which is overtaking the fainter first one. However, our interpretation is that, after the HI data gap, the faster LASCO event has already overtaken and passed the 24 January CME. Thus, at least the southern branch of the leading arch-shaped front in HI-2A and SMEI Camera 3 is the leading edge of the faster CME, whereas the bright feature, Event 1, is mostly from the slower LASCO CME on 24 January. It is possible that this structure is so bright because of the superposition or actual merging of material from both CMEs. We emphasize that our interpretation could only be made after assembling a complete data set and comparing it with modeling.

In terms of the kinematics of the events and examining just the HI and SMEI Camera 3 data points in Figure 6, it appears that a significant amount of deceleration is required to match the earlier, lower LASCO observations with those later and farther out, especially for the first, slower LASCO CME. This conclusion was also made by Harrison *et al.* (2008) for the HI observations after the data gap and out to $\sim 30^\circ$ elongation. This seems to be the case in our data out to at least 50° – 60° .

5. Discussion and Conclusions

This study represents the first multi-observatory analysis of ICMEs viewed in white light in the inner heliosphere, and compares a group of popular heliospheric models, each based on

different (and often contradictory) assumptions about the ICME evolution. We have demonstrated that combining data from the HI and SMEI instruments adds an abundance of information on a given event. SMEI, in particular, extends the FoVs of the HIs in both PA extent and elongation range. We note that more of the southern extension of the ICME structures was detected in SMEI, but not by the HIs, nor were the two arc features observed in SMEI Camera 2 well beyond the HI FoVs. Thus, the SMEI and HI data are complementary to each other. The HI-1 FoV fills the distance gap between the LASCO and COR FoVs near the Sun and the SMEI inner camera FoV. The HI-2 FoV overlaps with that of the SMEI Camera 3 over tens of degrees elongation and has better spatial resolution. SMEI observes nearly the entire sky, whereas the HI-2 FoVs are limited in latitude to a $\pm 35^\circ$ angle, which since April 2007, has been centered on the ecliptic. However, the HI data are free of the particle obscurations that SMEI suffers in Earth orbit.

The results of this study demonstrate the importance of understanding the large scales of ICMEs and the space through which they propagate, especially their 3D nature and interactions with the existing or background structures. The ICME structures in this study were observed with a combination of EIT and EUVI telescopes, the LASCO C2/C3 and SECCHI COR coronagraphs, and the HI-1A and HI-2A and SMEI heliospheric imagers out to $\sim 50^\circ$ elongation. Similar structures and orientations were observed within the regions of overlap. With SMEI we were able to track ICME structures out to $\sim 100^\circ$.

This study also demonstrates the complications introduced in the analysis of ICMEs observed by these instruments over such large distance ranges. Our study has shown the importance of making measurements along the same trajectories when combining data from different instruments and/or models. The brightness and structure of an ICME observed by an instrument along a given line of sight depends on its expansion, distance from the Sun, distance from the observing instrument, and distance from the Thomson surface. Not only are projection effects crucial, but also the effects of the geometry of the ICME. To correctly understand the images and produce physically meaningful measurements, it is important to understand the nature of the leading edge measurements from an evolving ICME, *e.g.*, the observed and actual leading edges may not coincide. This requires knowledge of both the geometry and trajectory of the structure. In addition, the assumption is usually made that the material moves radially from the Sun which may not always be true.

The analysis of the present events was also complicated by several specific factors. The most significant are: *i)* The HI data gap throughout 25 January. This covered the crucial period when the ICMEs moved from the FoV of HI-1 into that of HI-2, and when the faster CME may have overtaken the slower one. Hence, it was impossible to make a clear connection between the events observed by the two instruments. By the time the data returned, there were at least five separate structures in HI-2 where there was only a single structure in HI-1. Judging by the trajectories predicted by the two models, this gap also occurred in the region where any interaction between these two events would likely have begun. *ii)* Obscured areas in the SMEI data prevented elongation measurements of most of the SMEI events at the same PA as the measurements from the other instruments. The measurements for the SMEI event on 29 January, for example, varied by up to 65° from those made near the equatorial plane. This may cast some doubt on the validity of associating the HI-2 measurements with this particular SMEI event, although the 3D reconstruction data seem to support it. *iii)* Obscuration due to the dust and plasma from the extraordinary tail of Comet McNaught certainly affected our ability to track the faint ICME plasma in white-light wavelengths in both the HI and SMEI FoVs. This was especially so in the crucial region south of the ecliptic plane and in the southeast quadrant as viewed by SMEI. *iv)* Conversion techniques from distance to elongation may require more work. In this study we have used simple assumptions, from

the basic cone model to physically measuring angles using images and basic geometry. We acknowledge that some uncertainty may be introduced because of this technique.

Encouraging results from this paper are that the four models used for these events generally agree on both the kinematic evolution and appearance of the events. The kinematic results from the drive + drag model, HAFv2, and ENLIL all indicate that the first slower LASCO CME matched with the SMEI Camera 3 and HI Event1 (and maybe also Events 2 and 3) data and, later, with S3 (Camera 2) on 29 January. The second faster LASCO CME possibly overtook the first CME during the HI data gap and was tracked as the H2-0 ($PA = 90$) front observed by SMEI as S2 on 27 January. However, despite the results from HAFv2 and ENLIL showing merging of the two ICMEs, we are uncertain of this conclusion. Perhaps a partial interaction between the two events occurred, or what we observe is merely the superposition of separate structures along the line of sight.

All three of the kinematic/MHD models used to simulate the January events used the same magnetogram and WSA model inputs to produce a realistic solar wind background. These included a heliospheric current sheet, polarity boundaries and slow and high speed streams. All the model runs show severe distortions involving compressions and rarefactions of these ambient structures as the shock/ejecta material propagates outwards. Lugaz *et al.* (2008) note from their simulation that a third bright structure visible in their simulation on 26 January may have had an HI-2A counterpart. They conclude that this feature arose from compression of a preexisting dense stream (a high speed/slow speed wind boundary) by the ICMEs as viewed along that line of sight. It is possible that such an interaction could be misinterpreted as an ICME front, but we would expect it to travel much more slowly outward than the structures that we measured. Lugaz *et al.*'s study does, however, reinforce what others have shown, that accounting for the influence of solar wind background structures on ICME propagation can be important, and that 3D simulations can play an important role in understanding the kinematics over such large distances.

No metric radio type II bursts, indicating coronal shocks, were recorded on 24–25 January. However, as shown in Table 1, both the Wind WAVES and STEREO SWAVES (*e.g.*, Bougeret *et al.*, 2008) experiments detected a so-called decametric–hectometric (DH) type II burst associated with the 25 January event. Such type IIs are indicative of interplanetary shocks propagating beyond $\sim 10 R_s$ (Gopalswamy *et al.*, 2005). We note that both the HAF and ENLIL models suggest that the flank of the merged shock and/or ejecta might have reached Earth on 28 or 29 January. However, we could find no evidence of any shock or ejecta signatures in the ACE data, although the sector boundary crossing indicated by the models is evident on 29 January.

We emphasize the importance of using both observations and models to better understand the structure and propagation of ICMEs. The models help us to understand the gross propagation characteristics involved in interplanetary shocks, overall kinematics, and interactions both between ICMEs and with the background solar wind structures. The observations help to constrain the models and adjust key parameters of the models, such as their initial conditions, geometry, and speed.

Finally, during this period the STEREO spacecraft were still very near Earth with a minimal separation angle. We emphasize that this is the only period during the STEREO mission when both the SMEI and STEREO views of the inner heliosphere coincided. We need to study events combining both SMEI and HI observations of ICMEs at later times when the increasing separation angles permit us to make better use of the stereo aspect of the STEREO mission. We are working on several such studies and the results will be published in the future.

Acknowledgements We acknowledge P.P. Hick and A. Buffington for their efforts in the calibration and processing of SMEI data at UCSD. We thank C. Eyles of the University of Birmingham, UK, for SECCHI HI data, J. Davies of the Rutherford Appleton Laboratory for HI image processing, and V. Kunkel of NRL for SECCHI distance–time measurements. SMEI is a collaborative project of the US Air Force Research Laboratory, NASA, the University of California at San Diego, the University of Birmingham, UK, Boston College, and Boston University. Financial support has been provided by the Air Force, the University of Birmingham, and NASA. The Heliospheric Imager (HI) instrument was developed by a collaboration that included the Rutherford Appleton Laboratory and the University of Birmingham, both in the United Kingdom, the Centre Spatial de Liège (CSL), Belgium, and the US Naval Research Laboratory (NRL), Washington DC, USA. The STEREO/SECCHI project is an international consortium of the Naval Research Laboratory (USA), Lockheed Martin Solar and Astrophysics Lab (USA), NASA Goddard Space Flight Center (USA), Rutherford Appleton Laboratory (UK), University of Birmingham (UK), Max-Planck-Institut für Sonnensystemforschung (Germany), Centre Spatial de Liège (Belgium), Institut d’Optique Théorique et Appliquée (France), and Institut d’Astrophysique Spatiale (France). We also acknowledge use of the CME catalog that is generated and maintained at the CDAW Data Center by NASA and The Catholic University of America in cooperation with the Naval Research Laboratory. SOHO is a project of international cooperation between ESA and NASA. This work was supported for each coauthor by these sources: T.A.H. by the National Research Council Fellowship Program, funded by AFOSR contract F49620-02C-0015; B.V.J. and M.M.B. at UCSD by AFRL contract FA9550-06-1-0107, NSF grant ATM-0331513 and NASA grant NNG05GG45G; D.F.W., T.A.K. and D.R.M. at Boston College by AFRL contract FA8718-06-C-0015; S.J.T. under contract F61775-02-WE043 to the University of Birmingham; and C.D.F. at EXPI by AURA contract C10562N. D.F.W., T.A.H. and B.V.J. also were supported by NASA grant NNG05GF98G, and D.F.W. by Navy grants N00173-01-1-G013 and N00173-07-1-G016. D.O. was supported by AFOSR/MURI, NASA/LWS, and NSF/CISM grants.

References

- Ananthakrishnan, S., Tokumaru, M., Kojima, M., Balasubramanian, V., Janardhan, P., Manoharan, P.K., Dryer, M.: 1999, In: Habbal, S., *et al.* (eds.) *Solar Wind Nine, AIP Conf. Proc.* **471**, 321.
- Arge, C.N., Pizzo, V.: 2000, *J. Geophys. Res.* **105**, 10 465.
- Biesecker, D.A., Myers, D.C., Thompson, B.J., Hammer, D.M., Vourlidas, A.: 2002, *Astrophys. J.* **569**, 1009.
- Billings, D.E.: 1966, *A Guide to the Solar Corona*, Academic Press, New York.
- Bisi, M.M., Jackson, B.V., Hick, P.P., Buffington, A., Odstrcil, D., Clover, J.M.: 2008, *J. Geophys. Res.* **113**, A00A11. doi:[10.1029/2008JA013222](https://doi.org/10.1029/2008JA013222).
- Bougeret, J.-L., Goetz, K., Kaiser, M.L., Bale, S.D., Kellogg, P.J., Maksimovic, M., *et al.*: 2008, *Space Sci. Rev.* **136**, 487.
- Brueckner, G.E., Howard, R.A., Koomen, M.J., Korendyke, C.M., Michels, D.J., Moses, J.D., *et al.*: 1995, *Solar Phys.* **162**, 357.
- Buffington, A., Morrill, J.S., Hick, P.P., Howard, R.A., Jackson, B.V., Webb, D.F.: 2007, *Proc. SPIE* **6689**, 66890B, 1. doi:[10.1117/12.734658](https://doi.org/10.1117/12.734658).
- Cargill, P.J.: 2004, *Solar Phys.* **221**, 135.
- Chen, J.: 1996, *J. Geophys. Res.* **101**, 27 499.
- Delaboudinière, J.-P., Artzner, G.E., Brunaud, J., Gabriel, A.H., Hochedez, J.F., Millier, F., *et al.*: 1995, *Solar Phys.* **162**, 291.
- Dryer, M.: 1994, *Space Sci. Rev.* **67**, 363.
- Eyles, C.J., Simnett, G.M., Cooke, M.P., Jackson, B.V., Buffington, A., Hick, P.P., Waltham, N.R., King, J.M., Anderson, P.A., Holladay, P.E.: 2003, *Solar Phys.* **217**, 319.
- Eyles, C.J., Harrison, R.A., Davis, C.J., Waltham, N.R., Shaughnessy, B.M., Mapson-Menard, H.C.A., *et al.*: 2009, *Solar Phys.* **254**, 387. doi:[10.1007/s11207-008-9299-0](https://doi.org/10.1007/s11207-008-9299-0).
- Fry, C.D., Sun, W., Deehr, C.S., Dryer, M., Smith, Z., Akasofu, S.-I., Tokumaru, M., Kojima, M.: 2001, *J. Geophys. Res.* **106**, 20985.
- Fry, C.D., Dryer, M., Deehr, C.S., Sun, W., Akasofu, S.-I., Smith, Z.: 2003, *J. Geophys. Res.* **108**. doi:[10.1029/2002JA009474](https://doi.org/10.1029/2002JA009474).
- Fulle, M., Leblanc, F., Harrison, R.A., Davis, C.J., Eyles, C.J., Halain, J.P., *et al.*: 2007, *Astrophys. J.* **661**, L93.
- Gopalswamy, N., Auilar-Rodriguez, E., Yashiro, S., Nunes, S., Kaiser, M.L., Howard, R.A.: 2005, *J. Geophys. Res.* **110**, A12S07. doi:[10.1029/2005JA011158](https://doi.org/10.1029/2005JA011158).
- Hakamada, K., Akasofu, S.-I.: 1982, *Space Sci. Rev.* **31**, 3.

- Harrison, R.A., Davis, C.J., Eyles, C.J., Bewsher, D., Crothers, S.R., Davies, J.A., *et al.*: 2008, *Solar Phys.* **247**, 171. doi:[10.1007/s11207-007-9083-6](https://doi.org/10.1007/s11207-007-9083-6).
- Harrison, R.A., Davis, C.J., Bewsher, D., Davies, J.A., Eyles, C.J., Crothers, S.R.: 2009, *Adv. Space Res.*, submitted.
- Hewish, A., Scott, P.F., Wills, D.: 1964, *Nature* **203**, 1214.
- Hick, P.P., Buffington, A., Jackson, B.V.: 2005, In: *Proc. SPIE* **59011B**. doi:[10.1117/12.617996](https://doi.org/10.1117/12.617996).
- Hick, P.P., Buffington, A., Jackson, B.V.: 2007, In: *Proc. SPIE* **66890C**, 1. doi:[10.1117/12.734808](https://doi.org/10.1117/12.734808).
- Howard, R.A., Moses, J.D., Vourlidas, A., Newmark, J.S., Socker, D.G., Plunkett, S.P., *et al.*: 2008, *Space Sci. Rev.* **136**, 67.
- Howard, T.A., Simnett, G.M.: 2008, *J. Geophys. Res.* **113**, A08102. doi:[10.1029/2007JA012920](https://doi.org/10.1029/2007JA012920).
- Howard, T.A., Tappin, S.J.: 2009, *Space Sci. Rev.*, submitted.
- Howard, T.A., Webb, D.F., Tappin, S.J., Mizuno, D.R., Johnston, J.C.: 2006, *J. Geophys. Res.* **111**, A04105. doi:[10.1029/2005JA011349](https://doi.org/10.1029/2005JA011349).
- Howard, T.A., Fry, C.D., Johnston, J.C., Webb, D.F.: 2007, *Astrophys. J.* **667**, 610.
- Jackson, B.V.: 1992, In: Fischer, S., Vandas, M. (eds.) *Proceedings of the First SOLTIP Symposium, Liblice, Czechoslovakia*, Astronomical Institute of the Czechoslovak Academy of Sciences, Prague.
- Jackson, B.V., Buffington, A., Hick, P.P., Altrrock, R.C., Figueroa, S., Holladay, P.E., *et al.*: 2004, *Solar Phys.* **225**, 177.
- Jackson, B.V., Buffington, A., Hick, P.P., Wang, X., Webb, D.: 2006, *J. Geophys. Res.* **111**, A04S91. doi:[10.1029/2004JA010942](https://doi.org/10.1029/2004JA010942).
- Jackson, B.V., Bisi, M.M., Hick, P.P., Buffington, A., Clover, J.M., Sun, W.: 2008, *J. Geophys. Res.* **113**, A00A15. doi:[10.1029/2008JA013224](https://doi.org/10.1029/2008JA013224).
- Jones, R.A., Canals, A., Breen, A.R., Fallows, R.A., Bisi, M.M., Lawrence, G.: 2007, *J. Geophys. Res.* **112**, A08107. doi:[10.1029/2006JA011875](https://doi.org/10.1029/2006JA011875).
- Kahler, S.W., Webb, D.F.: 2007, *J. Geophys. Res.* **112**, A09103. doi:[10.1029/2007JA012358](https://doi.org/10.1029/2007JA012358).
- Kaiser, M.K., Kucera, T.A., Davila, J.M., St. Cyr, O.C., Guhathakurta, M., Christian, E.: 2008, *Space Sci. Rev.* **136**, 5.
- Leighly, J.B.: 1955, *Geogr. Rev.* **45**, 246.
- Lugaz, N., Manchester, W.B.IV, Roussev, I.I., Tóth, G., Gombosi, T.I.: 2007, *Astrophys. J.* **659**, 788.
- Lugaz, N., Vourlidas, A., Roussev, I.I., Jacobs, C., Manchester IV, W.B., Cohen, O.: 2008, *Astrophys. J.* **684**, L111.
- Manoharan, P.K., Ananthkrishnan, S.: 1990, *Mon. Not. Roy. Astron. Soc.* **244**, 691.
- McKenna-Lawlor, S.M.P., Dryer, M., Kartalev, M.D., Smith, Z., Fry, C.D., Sun, W., Deehr, C.S., Kecskemeti, K., Kudela, K.: 2006, *J. Geophys. Res.* **111**, A11103. doi:[10.1029/2005JA011162](https://doi.org/10.1029/2005JA011162).
- Michalek, G., Gopalswamy, N., Yashiro, S.: 2003, *Astrophys. J.* **584**, 472.
- Odstroil, D., Riley, P., Linker, J.A., Lionello, R., Mikic, Z., Pizzo, V.J.: 2003, In: Wilson, A. (ed.) *Solar Variability as an Input to the Earth's Environment, Estec, The Netherlands, SP-535*, ESA, Noordwijk, 541.
- Odstroil, D., Pizzo, V.J., Linker, J.A., Riley, P., Lionello, R., Mikic, Z.: 2004, *J. Atmos. Solar-Terr. Phys.* **66**, 1311.
- Richter, I., Leinert, C., Planck, B.: 1982, *Astron. Astrophys.* **110**, 115.
- Sun, W., Deehr, C.S., Fry, C.D., Dryer, M., Smith, Z., Akasofu, S.-I.: 2008, *Space Weather* **6**, S03006. doi:[10.1029/2006SW000298](https://doi.org/10.1029/2006SW000298).
- St. Cyr, O.C., Plunkett, S.P., Michels, D.J., Paswaters, S.E., Koomen, M.J., Simnett, G.M., *et al.*: 2000, *J. Geophys. Res.* **105**, 18 169.
- Tappin, S.J.: 2006, *Solar Phys.* **233**, 233. doi:[10.1007/s11207-006-2065-2](https://doi.org/10.1007/s11207-006-2065-2).
- Tappin, S.J., Buffington, A., Cooke, M.P., Eyles, C.J., Hick, P.P., Holladay, P.E., *et al.*: 2004, *Geophys. Res. Lett.* **31**, L02802. doi:[10.1029/2003GL018766](https://doi.org/10.1029/2003GL018766).
- Thompson, B.J., Cliver, E.W., Nitta, N., Delannée, C., Delaboudinière, J.-P.: 2000, *Geophys. Res. Lett.* **27**, 1431.
- Vourlidas, A., Howard, R.A.: 2006, *Astrophys. J.* **642**, 1216.
- Vourlidas, A., Subramanian, P., Dere, K.P., Howard, R.A.: 2000, *Astrophys. J.* **534**, 456.
- Webb, D.F., Jackson, B.J.: 1990, *J. Geophys. Res.* **95**, 20 641.
- Webb, D.F., Mizuno, D.R., Buffington, A., Cooke, M.P., Eyles, C.J., Fry, C.D., *et al.*: 2006, *J. Geophys. Res.* **111**, A12101. doi:[10.1029/2006JA011655](https://doi.org/10.1029/2006JA011655).
- Webb, D.F., Howard, T.A., Fry, C.D., Kuchar, T.A., Mizuno, D.R., Johnston, J.C., Jackson, B.V.: 2009, *Space Weather*. doi:[10.1029/2008SW000409](https://doi.org/10.1029/2008SW000409).
- Wood, B.E., Howard, R.A., Plunkett, S.P., Socker, D.G.: 2009, *Astrophys. J.* **694**, 707. doi:[10.1088/0004-637X/694/2/707](https://doi.org/10.1088/0004-637X/694/2/707).

- Xie, H., Ofman, L., Lawrence, G.: 2004, *J. Geophys. Res.* **109**, A03109. doi:[10.1029/2003JA010226](https://doi.org/10.1029/2003JA010226).
- Yashiro, S., Gopalswamy, N., Michalek, G., St. Cyr, O.C., Plunkett, S.P., Rich, N.B., Howard, R.A.: 2004, *J. Geophys. Res.* **109**, A07105. doi:[10.1029/2003JA010282](https://doi.org/10.1029/2003JA010282).
- Zhao, X.-P.: 1992, *J. Geophys. Res.* **97**, 15 051.
- Zhao, X.-P., Plunkett, S.P., Liu, W.: 2002, *J. Geophys. Res.* **107**, A81223. doi:[10.1029/2001JA009143](https://doi.org/10.1029/2001JA009143).